Investigating the State Dependence of Cloud Feedback Using a Suite of Perturbed Parameter Ensembles

JIANG ZHU,[a] BETTE L. OTTO-BLIESNER,[a] ESTHER C. BRADY,[a] TRUDE EIDHAMMER,[a] ANDREW GETTELMAN,[a,b] RAN FENG,[c] AND CHRISTINA S. MCCLUSKEY[a]

[a] *NSF National Center for Atmospheric Research, Boulder, Colorado*
[b] *Pacific Northwest National Laboratory, Richland, Washington*
[c] *Department of Earth Sciences, University of Connecticut, Storrs, Connecticut*

(Manuscript received 5 December 2024, in final form 9 April 2025, accepted 24 April 2025)

ABSTRACT: The state dependence of cloud feedback—its variation with the mean state climate—has been found in many paleoclimate and contemporary climate simulations. Previous results have shown inconsistencies in the sign, magnitude, and underlying mechanisms of state dependence. To address this, we utilize a perturbed parameter ensemble (PPE) approach with fixed sea surface temperature (SST) in the Community Atmosphere Model, version 6. Our suites of PPEs span a wide range of global mean surface temperatures (GMSTs), with spatially uniform SST perturbations of −4, 0, 4, 8, 12, and 16 K from the preindustrial. The results reveal a nonmonotonic variation with GMSTs: Cloud feedback increases under both cooler and warmer-than-preindustrial conditions, with a rise of ~0.1 W m^{-2} K^{-1} under a 4-K colder climate and ~0.4 W m^{-2} K^{-1} under a 12-K warmer climate. This complexity arises from differing cloud feedback responses in high and low latitudes. In high latitudes, cloud feedback consistently rises with warming, likely driven by a moist adiabatic mechanism that influences cloud liquid water. The low-latitude feedback increases under both cooler and warmer conditions, likely influenced by changes in the lower-tropospheric stability. This stability shift is tied to nonlinearity in thermodynamic responses, particularly in the tropical latent heating, alongside potential state-dependent changes in tropical circulations. Under warmer-than-preindustrial conditions, the increase in cloud feedback with warming is negatively correlated with its preindustrial value. Our PPE approach takes the model parameter uncertainty into account and emphasizes the critical role of state dependence in understanding past and predicting future climates.

SIGNIFICANCE STATEMENT: This study focuses on how cloud feedback—one of the most uncertain aspects of climate change—varies as global temperatures rise. We found that the cloud feedback decreases at first with warming and then increases, showing significant variation. This complexity stems from nonlinear thermodynamics, such as the Clapeyron–Clausius relationship, which describes how temperature affects moisture in the atmosphere. Our results indicate that the cloud feedback depends on the level of global warming, which is a significant factor rooted in fundamental physics. Recognizing this dependence is important for studies that aim to interpret past climates and predict future climate changes.

KEYWORDS: Cloud radiative effects; Feedback; Climate models; Cloud parameterizations

1. Introduction

The cloud feedback describes the radiative effects of cloud changes induced by surface warming (or cooling) that in turn can either amplify or damp the initial surface temperature change. Strength of the cloud feedback is quantified using the cloud feedback parameter λ_{cld}, as a function of changes in the cloud-induced top-of-atmosphere (TOA) radiation effects (ΔCRE) and surface temperature (ΔT):

$$\lambda_{cld} = \Delta\text{CRE}/\Delta T. \quad (1)$$

The λ_{cld} depends on the changes in cloud macrophysical (such as coverage, height, and location) and microphysical (such as water content, phase partition, and particle number concentration and size) characteristics, as well as their interactions with thermodynamical, radiative, and dynamical processes across a range of spatial and temporal scales (e.g., Gettelman and Sherwood 2016). The cloud feedback is responsible for the spread of equilibrium climate sensitivity (ECS) in multiple generations of climate models (Caldwell et al. 2016; Vial et al. 2013; Zelinka et al. 2020). An improved understanding and modeling of the complicated physical processes that drive the cloud feedback is crucial for reducing uncertainties in climate sensitivity and future climate projection (Zelinka et al. 2017; Ceppi et al. 2017).

The cloud feedback varies in space and time and depends on the background climate state and details of surface temperature change. A useful way to investigate the variability is to approximately separate it into 1) the state dependence that is directly linked to mean state climate [such as the global mean surface temperature (GMST)] and 2) the pattern dependence that is related to the geographic pattern of the surface temperature change (Bloch-Johnson et al. 2021; Sherwood et al. 2020). The pattern dependence, in particular the sea surface temperature (SST) pattern effect, has been intensively investigated in the context of historical warming (Armour et al. 2013; Dong et al. 2019; Andrews and Webb 2018; Zhou et al. 2016). The west Pacific has warmed more than the east Pacific and the

Corresponding author: Jiang Zhu, jiangzhu@ucar.edu

DOI: 10.1175/JCLI-D-24-0686.1

Southern Ocean during the historical period, where the Earth system features more negative feedbacks than that from the future projection with greater warming in the east Pacific and high latitudes. As a result of the different SST patterns, observations of the historical forcing and temperature responses can lead to the underestimation of ECS. A proper accounting for the SST pattern effect in the historical constraint has contributed to the increase in the low-end estimation of ECS in the Intergovernmental Panel on Climate Change Assessment Report (IPCC 2023; Armour et al. 2024).

Different from the pattern dependence, state dependence of the cloud feedback relies only on the GMST and is more naturally studied in a paleoclimate context, given the much greater temperature variation in Earth's past. For example, GMST during the Cenozoic (the last 65 million years) varies by more than 20°C, which is approximately 20 times the historical warming since 1850 (Tierney et al. 2020; Hansen et al. 2013). State dependence of the cloud feedback has been suggested to be an essential element for the simulation of past hothouse climates (Caballero and Huber 2013; Zhu et al. 2019; Schneider et al. 2019; Abbot and Tziperman 2008) and has been found in high-CO_2 simulations based on the present-day climate (e.g., Meraner et al. 2013; Zhu and Poulsen 2020).

State dependence of the cloud feedback can be mathematically viewed as a derivative of the cloud feedback with respect to GMST, which indicates potentially greater uncertainty in our quantification and understanding than that of the cloud feedback itself. Previous modeling studies do not agree on the rate of change, e.g., abrupt nonlinear increase (Caballero and Huber 2013; Schneider et al. 2019) versus gradual linear increase with temperature (Zhu et al. 2019). In addition, mechanisms responsible for the state dependence remain elusive. In principle, state dependence in any cloud-feedback-related process may give rise to the state dependence of the cloud feedback. The near-exponential increase of atmospheric water vapor with temperature represents such a nonlinear mechanism. Water vapor can potentially produce the state dependence of the cloud feedback through changing 1) surface latent heat flux and mixing in the atmospheric boundary layer (BL), 2) the specific humidity gradient and entrainment between the free troposphere and BL, and 3) free-tropospheric downwelling longwave radiation and the impact on cloud-top cooling and BL stability (Bretherton 2015). In addition to water vapor, the changes in cloud-phase partitioning (the decrease of cloud ice content in mixed-phase clouds with warming) can lead to an increase of cloud feedback through weakening the negative cloud-phase feedback (Tan et al. 2016; Zhu and Poulsen 2020). Other potential mechanisms may involve radiation and large-scale dynamics (Caballero and Huber 2013; Henry and Vallis 2022) but, along with the mechanisms mentioned above, are in general much less studied. Moreover, quantification and mechanistic understanding of the state dependence have been confounded with changes in forcing and the geographical pattern of temperatures in previous studies owing to the substantial difference in model complexity and experimental design. Due partly to the large uncertainty in the state dependence of the cloud feedback, Sherwood et al. (2020) excluded the past hothouse climates such as the Paleocene–Eocene thermal maximum in the paleoclimate constraints on ECS but suggested that "Differentiating between state dependence in the radiative forcing, and in the feedbacks, could be an area of future progress."

Here, we investigate the state dependence of the cloud feedback using a perturbed parameter ensemble (PPE) with the Community Atmosphere Model, version 6 (CAM6). We focus on two questions: 1) How does the cloud feedback depend on the wide range of GMSTs that Earth has gone through during the Cenozoic? and 2) What can we learn about the mechanisms of state dependence? We use preindustrial-based atmosphere/land-only simulations with prescribed uniform warming/cooling in SST, which helps us to focus on the state dependence without complications from forcing and the pattern dependence. We use the PPE approach, which has been proven to be a useful approach to explore uncertainties in model physical parameterizations and gain deeper mechanistic understanding (e.g., Gettelman et al. 2024).

This study focuses on the state dependence of cloud feedback, whereas analysis and parametric sensitivity on the present-day cloud feedback can be found in previous studies with a similar model and approach (Duffy et al. 2024; Eidhammer et al. 2024; Gettelman et al. 2024). The PPE approach and the experimental setup, along with the calculation of the cloud feedback, are described in section 2. The results of the state dependence are presented in section 3. Mechanistic understanding is presented in section 4. We discuss and conclude in section 5.

2. Model, simulation, and method

a. Model

We employ the CAM6 coupled with the Community Land Model, version 5, the model configuration that has been used for the PPE application to present-day and future climate (Duffy et al. 2024; Eidhammer et al. 2024; Gettelman et al. 2024). This version of CAM6 shares the same physical parameterizations and major tunings as the released version within the Community Earth System Model (CESM), version 2 (Danabasoglu et al. 2020; Gettelman et al. 2019), but has modifications in code and scripts to support PPE simulations. CAM6 uses a unified moist turbulence scheme, the Cloud Layers Unified By Binormals (CLUBB), for its atmospheric boundary layer, shallow convection, and cloud macrophysics schemes (Bogenschutz et al. 2013; Larson and Golaz 2005). The microphysical scheme is the Morrison and Gettelman, version 2 (MG2), which is a two-moment scheme that predicts the mass and number concentration of cloud and precipitation particles (Gettelman et al. 2015). CAM6 addresses the indirect aerosol effects and cloud–aerosol interactions through a coupling of MG2 with the four-mode modal aerosol model and the classical-theory-based heterogeneous ice nucleation scheme in mixed-phase clouds (Liu et al. 2016; Hoose et al. 2010; Wang et al. 2014). CAM6 uses the deep convection (ZM) by Zhang and McFarlane (1995). CAM6 has the capability to use online satellite simulators (COSP) to emulate satellite products to facilitate direct comparison and assessment with observations (Bodas-Salcedo et al. 2011).

We implement published fixes in the cloud microphysics and ice nucleation in CAM6 to address its high ECS and strong cloud feedback (Zhu et al. 2022). The standard CESM2 with CAM6 produces a high ECS (e.g., 6.1°C from a doubling CO_2 experiment with a ~2°-resolution atmosphere coupled with a slab ocean) and unrealistically cold simulation of the Last Glacial Maximum (LGM) and excessively warm early Eocene (Zhu et al. 2021, 2020, 2022, 2024). The high ECS has been attributed to the cloud parameterization and feedback (Gettelman et al. 2019; Zhu et al. 2021). Zhu et al. (2022) developed fixes in the cloud microphysics and ice nucleation, which led to much reduced ECS (4.0°C) and a more realistic simulation of the LGM without compromising the present-day climate. The fixes include the removal of an inappropriate limiter on the cloud ice number concentration and the increase of microphysical substepping (shortening time step). The fixes represent a means to improve the physical and numerical aspects of the model (Shaw et al. 2022). Alternative fixes by Gettelman et al. (2023) without directly changing substepping are planned to be used in CESM3.

We run the land model, CLM5, in a simplified mode with prescribed satellite phenology (SP), in which the vegetation type, leaf area index, and canopy height are prescribed according to satellite observations. The SP mode excludes vegetation phenological feedback and helps us focus on the classical atmospheric feedbacks.

b. *Perturbed parameter ensemble*

We set up the paleoclimate PPE (paleoPPE) simulations following the methodology of CAM6 PPE (cam6PPE) (Eidhammer et al. 2024). We perturb 45 parameters in cloud microphysics (MG2), convection (CLUBB and ZM), and aerosol schemes. We use Latin hypercube sampling to create 250 sets of perturbed parameters that cover the entire range for each parameter and are uniformly distributed in the parameter space. Table 1 lists the parameter name, default value in the model, range in the PPE, and short description. For a detailed explanation of these parameters and the justification of their range, readers are referred to published work (Eidhammer et al. 2024).

The paleoPPE differs from cam6PPE in the following aspects. First, we implement the fixes in cloud microphysics and ice nucleation to have overall more realistic cloud feedback (assessed according to paleoclimate data; see section 2a). Second, we use a lower horizontal resolution (~2° vs ~1°), which reduces the computing and storage demand and allows longer simulations (5 vs 3 yr). Third, as a result of the lower horizontal resolution, the default parameter values in the unperturbed model were tuned differently, including a smaller MG2_DCS, dust emission factor, and CLUBB_gamma and a larger sea salt emission scaling (Table 1). Fourth, paleoPPE uses C11b and a wider parameter range in CLUBB_C8, which are found to impact the cloud feedback in our exploratory simulations (not shown). A wider range of CLUBB_C8 has also been used in the calibration of Energy Exascale Earth System Model (E3SM), which shares many atmospheric parameterizations with CESM2 (Ma et al. 2022). Fifth, paleoPPE uses the preindustrial boundary condition, different from the present-day condition in cam6PPE (2000 AD). All parameter-related differences from cam6PPE are highlighted in Table 1 with bold and italic fonts. Note that parameters in paleoPPE are regenerated using Latin hypercube sampling and different from those in cam6PPE.

Multiple suites of PPE simulations are performed with different SST and sea ice conditions, including the preindustrial and those with uniform SST change of −4, +4, +8, +12, and +16 K, as well as an additional set with a warming magnitude of +4 K in global mean with spatial pattern derived from the abrupt 4xCO_2 simulation between years 131 and 150 (Zhu et al. 2022). The preindustrial SST and sea ice coverage are from Hurrell et al. (2008). For the PPE suites with relatively small SST change (−4 to +8 K), sea ice coverage is fixed at the preindustrial values. To increase the realism and numerical stability of the simulations with a large magnitude of warming (+8 to +16 K), we remove sea ice and prescribe the same uniform SST change as the nonsea ice region (Table 2). As a result, we have two suites of PPEs with 8-K warming that differ in the sea ice–covered regions and can be used to separate the impacts from the replacement of sea ice with a regional warming of 8 K. In the analysis presented here, we use the pair of simulations with the same sea ice conditions to compute the cloud feedback due to a 4-K warming (e.g., P04K versus P08K, and P08K_NOICE versus P12K_NOICE). We note that the nonlocal impact of sea ice treatment on clouds is relatively small (P08K vs P08K_NOICE; not shown). For simplicity, land ice sheets are not changed, as they cover a smaller area and have less impact on the overall model stability. In sum, a total of eight suites of PPE simulations ($8 \times 250 =$ 2000 ensembles and a total of 10 000 model years) are performed (data of a ninth suite with only 4xCO_2 forcing is also published but not discussed in this paper; Table 2). Simulations with the default parameter values are also carried out as a reference (referred to as the default model hereafter). The final 4 years of the simulation are analyzed to minimize the impact of potential drift during spinning up the atmosphere.

c. *Calculation of the cloud feedback parameter*

In this study, we define the cloud feedback λ of a certain climate state as the cloud radiative contribution R_{CLD} scaled by the global mean warming in a pair of simulations with 4-K warming. Take the P04K state as an example,

$$\lambda_{P04K} = (R_{CLD\_P08K} - R_{CLD\_P04K})/(T_{P08K} - T_{P04K}). \quad (2)$$

We calculate R_{CLD} and therefore λ using multiple methods including the simple calculation with model output of cloud radiative effects (CREs; λ_{CRE}), the approximated partial radiative perturbation (APRP; λ_{APRP}), and the radiative kernels $\lambda_{kernels}$. Each method is known to have strengths and weaknesses. The λ_{CRE} is simple to compute but can be biased by the masking effects from other radiative processes (Soden et al. 2008). The $\lambda_{kernels}$ can depend on the choices of the kernels and relies on assumptions of small perturbations and linearity, which may not hold in our simulations with large magnitude of temperature changes. The λ_{APRP} is accurate (error $< 10\%$) and simpler than the sophisticated PRP method but only

TABLE 1. List of parameters, description, default values, and the perturbed range (group by schemes, moist turbulence, microphysics, aerosol, and deep convection, respectively). Bold and italic font means the parameter differs from Eidhammer et al. (2024). Notation: u, v, and w denote east–west, north–south, and vertical velocity, respectively; θ_l, liquid water potential temperature; and r_t, total water mixing ratio.

Parameter name	Description (units when applicable)	Default	Min	Max
clubb_c1	Dissipation of variance of w	1.0	0.4	3
clubb_c2rt	Dissipation of variance of r_t	1.0	0.2	2
clubb_c6rt	Newtonian damping of r_t flux at low skewness	4.0	2.0	6
clubb_c6rtb	Newtonian damping of r_t flux at high skewness	6.0	2.0	8
clubb_c6thl	Newtonian damping of θ_l flux at low skewness	4.0	2.0	6
clubb_c6thlb	Newtonian damping of θ_l flux at high skewness	6.0	2.0	8
clubb_c8	Newtonian damping of skewness of w	4.2	1.0	***7***
clubb_c11b	***Buoyancy damping of skewness of w***	***0.7***	***0.2***	***0.8***
clubb_c14	Newtonian damping of variance of u and v	2.2	0.4	3
clubb_beta	Coefficient controlling skewness of θ_l and r_t	2.4	1.6	2.5
clubb_gamma_coef	Constant of the width of PDF in w coordinate	***0.275***	0.25	0.35
clubb_c_k10	Momentum diffusion factor	0.5	0.2	0.6
clubb_wpxp_l_thresh	Length scale threshold below which extra damping is applied to C6 and C7 (m)	60	20	200
micro_mg_accre_enhan_fact	Accretion enhancement factor	1.0	0.1	10.0
micro_mg_autocon_fact	Autoconversion factor	0.01	0.005	0.2
micro_mg_autocon_lwp_exp	Liquid water exponent coefficient for autoconversion	2.47	2.10	3.30
micro_mg_autocon_nd_exp	Droplet number exponent coefficient for autoconversion	−1.1	−0.8	−2
micro_mg_berg_eff_factor	Bergeron efficiency factor	1.0	0.1	1.0
micro_mg_dcs	Size threshold for ice–snow autoconversion (m)	***2×10^{-4}***	5×10^{-5}	1×10^{-3}
micro_mg_effi_factor	Scaling factor for effective radius for optics calculation	1.0	0.1	2.0
micro_mg_homog_size	Homogeneous freezing ice particle size (m)	2.5×10^{-5}	1×10^{-5}	2×10^{-4}
micro_mg_iaccr_factor	Scaling factor for ice–snow accretion	1.0	0.2	1.0
micro_mg_max_nicons	Maximum allowed ice number concentration (kg^{-1})	1×10^{8}	1×10^{5}	1×10^{10}
micro_mg_vtrmi_factor	Scaling factor for cloud ice fall speed	1.0	0.2	5.0
microp_aero_npccn_scale	Scaling factor for activated liquid number	1	0.33	3
microp_aero_wsub_min	Minimum subgrid velocity for liquid activation ($m\ s^{-1}$)	0.2	0	0.5
microp_aero_wsub_scale	Scaling factor for subgrid velocity for liquid activation	1	0.1	5
microp_aero_wsubi_min	Minimum subgrid velocity for ice activation ($m\ s^{-1}$)	0.001	0	0.2
microp_aero_wsubi_scale	Scaling factor for subgrid velocity for ice activation	1	0.1	5
dust_emis_fact	Tuning parameter for dust emission	***0.55***	0.1	1.0
seasalt_emis_scale	Tuning parameter for sea-salt emission	***1.1***	0.5	2.5
sol_factb_interstitial	Tuning parameter for below-cloud aerosol scavenging	0.1	0.1	1
sol_factic_interstitial	Tuning parameter for in-cloud aerosol scavenging	0.4	0.1	1
cldfrc_dp1	Deep convection cloud fraction parameter	0.1	0.05	0.25
cldfrc_dp2	Deep convection cloud fraction parameter	500	100	1000
zmconv_c0_lnd	Convective precipitation efficiency over land (m^{-1})	0.0075	0.002	0.1
zmconv_c0_ocn	Convective precipitation efficiency over ocean (m^{-1})	0.03	0.02	0.1
zmconv_capelmt	Triggering threshold for deep convection ($J\ kg^{-1}$)	70	35	350
zmconv_dmpdz	Convective parcel fractional mass entrainment rate (m^{-1})	-1×10^{-3}	-2×10^{-3}	-2×10^{-4}
zmconv_ke	Convective evaporation efficiency ($kg^{0.5}\ m^{-1}\ s^{-1.5}$)	5×10^{-6}	1×10^{-6}	1×10^{-5}
zmconv_ke_lnd	Convective evaporation efficiency land ($kg^{0.5}\ m^{-1}\ s^{-1.5}$)	1×10^{-5}	1×10^{-6}	1×10^{-5}
zmconv_momcd	Convective momentum transport parameter (downward)	0.7	0	1
mconv_momcu	Convective momentum transport parameter (upward)	0.7	0	1
zmconv_num_cin	Allowed number of negative buoyancy crossings	1	1	5
zmconv_tiedke_add	Initial convective parcel temperature perturbation (K)	0.5	0	2

quantifies the shortwave component (Taylor et al. 2007). The λ_{APRP} could be superior to $\lambda_{\mathrm{kernels}}$ for shortwave due to the sensitivity of $\lambda_{\mathrm{kernels}}$ to choices of kernels.

Our analysis focuses on the state dependence ($\Delta\lambda$ between two climate states) and is found to be insensitive to choices of the method (Fig. 1). For example, shortwave λ_{CRE} correlates strongly with λ_{APRP} ($r = 1.00$) but is on average biased by $-0.15\ \mathrm{W\ m^{-2}\ K^{-1}}$ under the preindustrial background state (Fig. 1a), while $\Delta\lambda_{\mathrm{CRE}}$ between the preindustrial and a 4-K warmer or colder state is the same as $\Delta\lambda_{\mathrm{APRP}}$ within the uncertainty (Figs. 1e,i). Similarly, longwave λ_{CRE} correlates strongly with $\lambda_{\mathrm{kernels}}$ ($r = 0.95$) but is systematically lower by $0.64\ \mathrm{W\ m^{-2}\ K^{-1}}$ (Fig. 1c), while $\Delta\lambda_{\mathrm{CRE}}$ is the same as $\Delta\lambda_{\mathrm{kernels}}$ within uncertainty (Figs. 1g,k). A small difference exists between shortwave $\Delta\lambda_{\mathrm{CRE}}$ and $\Delta\lambda_{\mathrm{kernels}}$ (Figs. 1f,j), which could be due to the partial neglect of state dependence of the kernels method. In the remainder of the paper, we use $\Delta\lambda_{\mathrm{CRE}}$ to study the state dependence with $\Delta\lambda_{\mathrm{APRP}}$ used for the cross

TABLE 2. A list of PPE simulations performed in this study. Information includes the experiment name, global mean SST change (ΔSST) based on PREI, whether the SST change has a spatial pattern, sea ice conditions, as well as the mean and standard deviation of the GMST in each ensemble. Each ensemble has 250 PPE simulations and one simulation with the default parameter setting. Each simulation is run for five model years.

Experiment name	Mean ΔSST (K)	Uniform ΔSST	Sea ice	GMST and ΔGMST (°C)
PREI	0	Yes	Preindustrial	14.6
M04K	−4	Yes	Preindustrial	−4.1
P04K	+4	Yes	Preindustrial	+4.2
P08K	+8	Yes	Preindustrial	+8.5
P08K_NOICE	+8	Yes	Removed	+9.7
P12K_NOICE	+12	Yes	Removed	+14.2
P16K_NOICE	+16	Yes	Removed	+18.8
P04K_PAT	+4	No	Preindustrial	+4.1
PREI_4xCO_2	0	—	Preindustrial	+0.5

examination of the shortwave component. We use λ_{kernels} to compare the preindustrial values against the other models from phases 5 and 6 of the Coupled Model Intercomparison Project (CMIP), as well as the expert assessment (Sherwood et al. 2020; Zelinka et al. 2022).

d. *Assessment of cloud fields and feedback*

To ensure the overall realistic results on the state dependence, we focus the analysis on more plausible PPE members based on their simulation of the preindustrial cloud fields and feedback in observations and expert assessments. PPE members could be implausible because preindustrial (PREI) simulations have not been retuned. Furthermore, although PPE uses parameter ranges according to expert judgment regarding their physical limits, the combinations of different parameters are not necessarily realistic. State dependence from these implausible members could be much less relevant to the real world. We use gridded satellite observations to assess the representation of clouds in PREI, including the cloud fraction from the International Satellite Cloud Climatology Project (ISCCP; 60°S–60°N) H-Series (Rossow et al. 2022) and the cloud radiative effects from the Clouds and the Earth's Radiant Energy System (CERES) Energy Balanced and Filled (EBAF), edition 4.2 (Loeb et al. 2018). Data temporal coverages are from January 1999 to December 2016 and from March 2000 to February 2024, respectively. Additionally, we use the expert assessments of the total cloud feedback to evaluate the cloud feedback in PREI (Sherwood et al. 2020; Zelinka et al. 2022). We note that using modern observations to evaluate the preindustrial simulations is not ideal, but this should have limited impact on our results, as the differences between PPE simulations (e.g., shown in Fig. 2) are in general much larger than the potential preindustrial–modern differences.

The cloud feedback derived from Atmospheric Model Intercomparison Project (AMIP) and amip-p4K simulations from available CMIP5 and CMIP6 models are used as a reference to compare with our PPE results from a single model (Zelinka et al. 2022). This comparison can also contextualize the parametric uncertainty in CAM6 within the structural uncertainty described by other CMIP models.

3. State dependence of the cloud feedback in paleoPPE

a. *Assessment of the preindustrial cloud and cloud feedback*

PaleoPPE generates a wide range of cloud and cloud feedback under the preindustrial condition (Fig. 2). Compared to satellite observations, RMSEs in the shortwave and longwave CREs and cloud fraction range from 8.3 to 44.9 W m^{-2}, from 3.4 to 26.6 W m^{-2}, and from 9.1% to 32.1%, respectively. Values in the default model ranked in the top five (8.7 W m^{-2}, 6.0 W m^{-2}, and 15.2%, respectively), highlighting the overall success of the expert tuning of the model during the development process. The cloud feedback λ_{kernels} ranges from 0.0 to 1.5 W m^{-2} K^{-1} with the default value of 0.36 W m^{-2} K^{-1}. The cloud feedback has a negligible correlation with the RMSEs in CREs (0.12 and 0.24; Figs. 2a,b) and weak negative correlation with RMSE in the cloud fraction (−0.39). These results suggest that efforts that aim to reduce error in the present-day clouds may not necessarily lead to reduced uncertainty in the cloud feedback. Many PPE members have RMSEs of cloud fields and the cloud feedback outside the range from the CMIP5 and CMIP6 models and WCRP assessments (Zelinka et al. 2020, 2022; Bock and Lauer 2024), illustrating that not all parameter combinations have good skill at simulating present-day clouds and the cloud feedback.

To remove the less plausible PPE members that may contaminate our results, we rank the PPE members using a combined metric that averages the standardized RMSEs of global mean cloud CREs and fraction and mean bias of the cloud feedback from the expert assessment. Based on this ranking, the top 50 members have RMSEs in cloud shortwave CREs of 8.3–20.3 W m^{-2}, longwave CREs of 3.7–8.5 W m^{-2}, and fraction of 9.2%–20.8%, respectively (Fig. 2; markers with darker color and white edge), which is comparable to values from the CMIP5 and CMIP6 models and other multiple model assessments (Bock and Lauer 2024; Medeiros et al. 2023). The persistent large bias across the PPE and CMIP models indicates a structural deficiency in the current generation of models. The total cloud feedback in the top 50 members ranges from 0.2 to 1.0 W m^{-2} K^{-1} with an ensemble mean of 0.6 W m^{-2} K^{-1} (calculated using PREI and P04K), which is also comparable to the range in the CMIP models and agrees better with the WCRP assessment (Fig. 3). We note that our choices of the metric to rank the PPE members aim to remove the implausible members and retain sufficient members for exploring the parameter uncertainty and providing good statistics. In addition, the top 50 members broadly exhibit a similar degree of biases in the cloud fields and range of the cloud feedback as the other CMIP5 and CMIP6 models. Our following analysis emphasizes the top 50 members, and any statistics are calculated from these members. The results on the state dependence of the cloud feedback do not depend much on details of the choice of the metrics (e.g.,

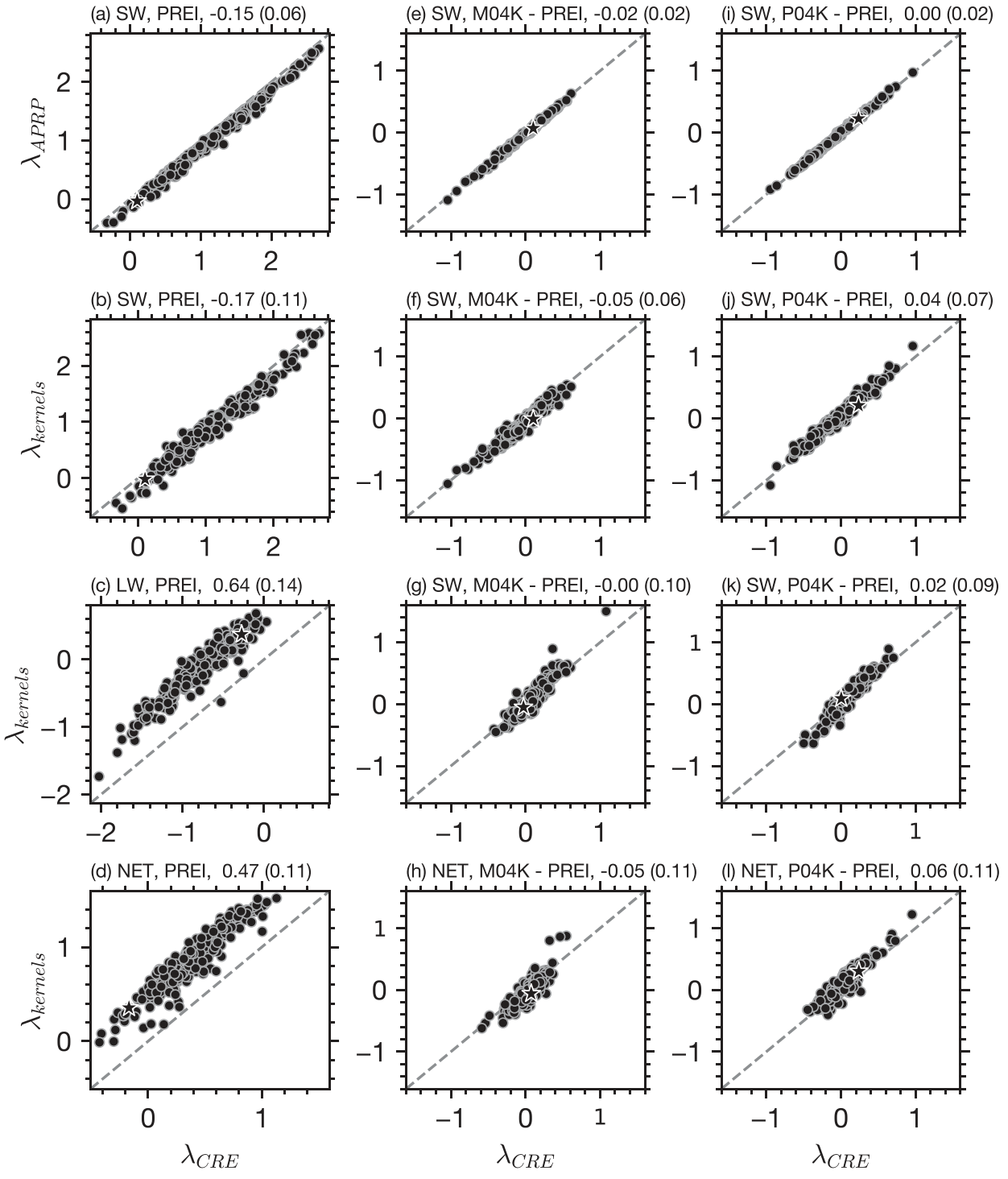

FIG. 1. Comparison of the cloud feedback calculated using the CRE (λ_{CRE}; x axis), the APRP (λ_{APRP}; y axis of first row; shortwave only), and the radiative kernels method ($\lambda_{\mathrm{kernels}}$; y axis of second row–fourth row for shortwave, longwave, and net, respectively). (left) The cloud feedback for the PREI climate. (middle) (right) The state dependence of cloud feedback at the 4-K colder and warmer climate states (M04K and P04K), respectively. Circle markers indicate the 250 PPE members, and the star denotes the simulation with the default parameters. Numbers in the subplot title are the ensemble mean difference and the standard deviation (in parentheses) between two calculations (W m^{-2} K^{-1}).

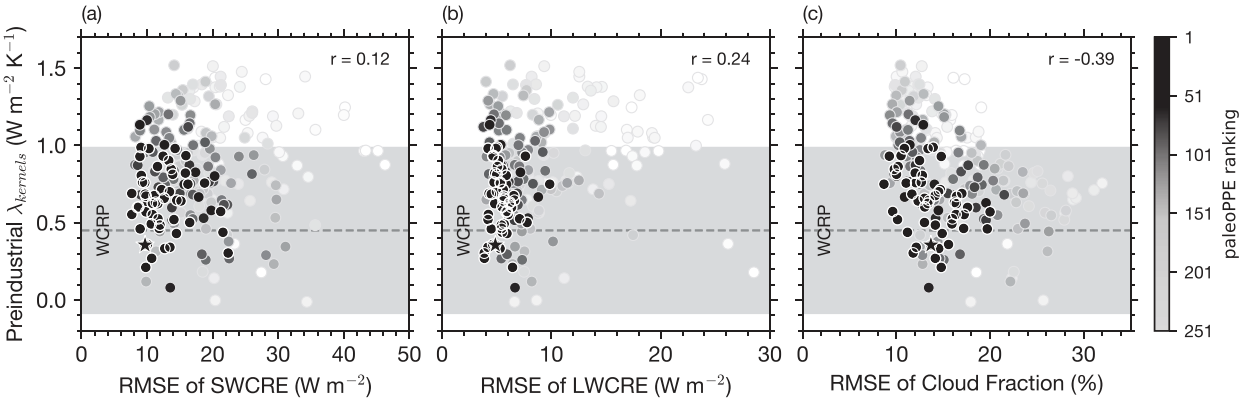

FIG. 2. Assessment of the simulation of cloud and cloud feedback under the PREI condition. Shown is the cloud feedback calculated using the kernels method (λ_{kernels} with PREI and P04K; y axis) against the RMSEs (x axis) in (a) the SWCRE, (b) LWCRE, and (c) cloud fraction. RMSEs in CREs and fraction are calculated by comparing them in PREI against the satellite observations. The dashed horizontal line indicates the central estimation of the cloud feedback from the WCRP expert assessment with the gray patch indicating the 90% interval (Sherwood et al. 2020; Zelinka et al. 2022). The PPE members are ranked according to the mean of standardized RMSEs and departure from the WCRP central estimation of the cloud feedback, as reflected by the face color of the markers in the plot. Circle markers indicate the 250 PPE members, and the star denotes the simulation with the default parameters. The correlation coefficient between the cloud feedback and RMSEs in the PPEs is also listed.

mean bias versus RMSE), as long as the analysis is focused on top-performed members.

For different cloud feedback components, paleoPPE in general matches the spread in CMIP and WCRP assessment well, especially the top 50 members (Fig. 3). The land cloud amount and midlatitude marine low-cloud amount feedbacks overlap with the WCRP assessment quite well. The high-cloud altitude feedback is stronger than that of the WCRP assessment (mean values of 0.4 W m^{-2} K^{-1} in the top 50 members vs 0.2 W m^{-2} K^{-1} in the WCRP assessment), which likely reflects

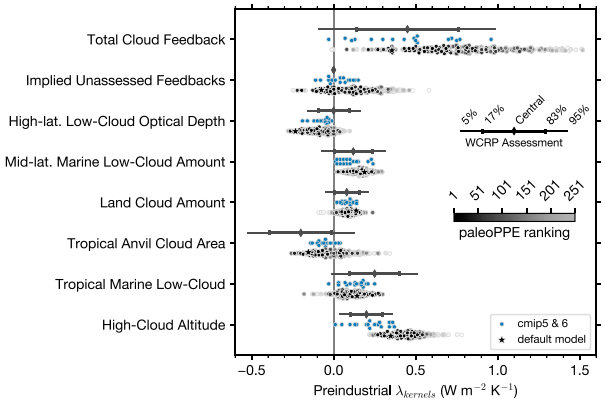

FIG. 3. Assessment of the simulation of cloud feedback components under the PREI condition. The cloud feedback and decomposition from the WCRP expert assessment are shown as the black horizontal lines with error bars indicating the one standard deviation and 90% confidence intervals (Sherwood et al. 2020; Zelinka et al. 2022). Circles are the cloud feedback from the 250 PPE members with the face color indicating their performance ranking by their agreement with the satellite observations of CREs and fraction, as well as the WCRP central estimation of the total cloud feedback. The star denotes the simulation with the default parameters. Blue circles are the results from the CMIP5 and CMIP6 models.

a deficiency in the simulation of tropical deep convection and/or ice clouds (Duffy et al. 2024). In addition, the tropical anvil cloud area feedback is higher than the WCRP assessment (mean values of −0.1 W m^{-2} K^{-1} in the top 50 members versus −0.2 W m^{-2} K^{-1} in WCRP assessment), which seems to agree with recent studies indicating a potential low bias in the WCRP assessment (McKim et al. 2024; Sokol et al. 2024). The tropical marine low-cloud feedback is at the lower end of the WCRP assessment (mean of 0.1 vs 0.25 W m^{-2} K^{-1}). The high-latitude optical depth feedback is somewhat lower than the WCRP assessment (mean of −0.1 vs 0.0 W m^{-2} K^{-1}). The top 50 members are overall comparable to that of CMIP5 and CMIP6 models, suggesting that PPE is an effective way to study the cloud feedback by accounting for uncertainties in model physics within a single climate model.

b. *State dependence of the cloud feedback in paleoPPE*

The global mean cloud feedback varies nonmonotonically with the background temperature with higher ensemble means under both colder and warmer than preindustrial conditions (Fig. 4a; top 50 members are shown). Under colder conditions (M04K), 44 of the top 50 members exhibit stronger cloud feedback than the corresponding members in PREI. On average, the cloud feedback in M04K is larger by 0.12 ± 0.12 W m^{-2} K^{-1} ($\Delta\lambda_{\text{CRE}}$). Under warmer states, the cloud feedback increases by 0.10 W m^{-2} K^{-1} in P04K and then further rises by 0.22 and 0.07 W m^{-2} K^{-1} in P08K and P12K, respectively. Compared with PREI, 46 of the top 50 members exhibit stronger cloud feedback in P12K, with an average increase of 0.38 ± 0.32 W m^{-2} K^{-1}. This nonmonotonic state dependence is also clear in individual members (thin gray lines in Fig. 4a).

The nonmonotonic state dependence in the cloud feedback results from distinct behaviors over different cloud regimes. Based on the zonal mean in Fig. 4b, 40°N/S seems to be a good threshold across the cold and very warm climates to

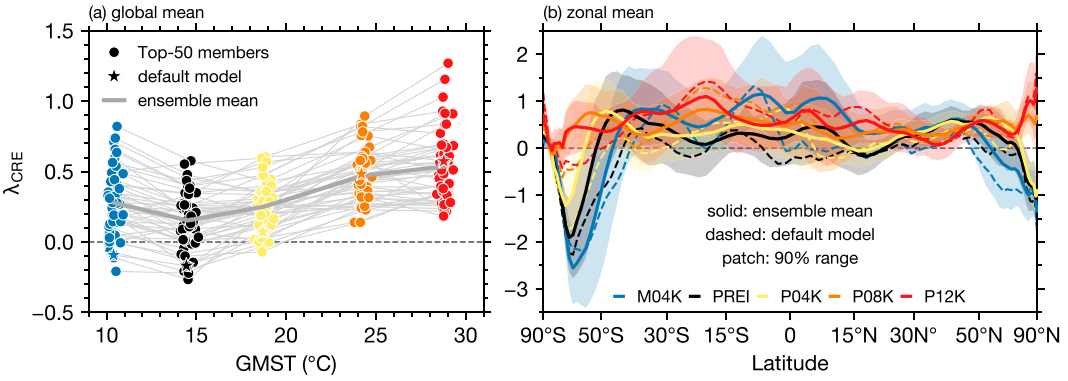

FIG. 4. (a) Global mean cloud feedback for the background states with uniform ΔSST of −4 K (M04K in blue), 0 K (PREI in black), 4 K (P04K in yellow), 8 K (P08K in orange), and 12 K (P12K in red) added to PREI. The cloud feedback parameter for a certain background state is calculated using the CRE method λ_{CRE} with the background state and the corresponding state with a uniform SST warming of 4 K. The same PPE members are connected using thin gray lines. (b) Zonal mean cloud feedback for various background states. The results are from the top 50 ensemble members (W m^{-2} K^{-1}).

generally separate the high and low latitudes that feature different behaviors. Over high latitudes (40°N/S poleward), all the members show a strengthening of the cloud feedback with warming that saturates at a GMST of ~24°C (see also Fig. 6a). The ensemble mean increases by 0.39 ± 0.16 W m^{-2} K^{-1} from M04K to P08K and stays largely unchanged in P12K (this value has been scaled by fraction area coverage such that it measures the net contribution to the global mean). Over low latitudes (40°S–40°N), cold climate (M04K; blue in Fig. 4b) has mean cloud feedback that is higher by 0.27 ± 0.12 W m^{-2} K^{-1} than the preindustrial, while warm climate (P12K; red in Fig. 4b) is also higher by 0.21 ± 0.26 W m^{-2} K^{-1} (see also Fig. 9a). All top 50 members show an increase in the low-latitude cloud feedback from PREI to M04K, whereas 40 of the 50 members show increases from PREI to P12K.

The overall coherence among individual members is quantitatively supported by the strong correlation with correlation coefficients of 0.86 and 0.74 between the preindustrial cloud feedback and that in M04K and P04K, respectively (Figs. 5a,b). The cloud feedback in P12K, however, exhibits minimal correlation

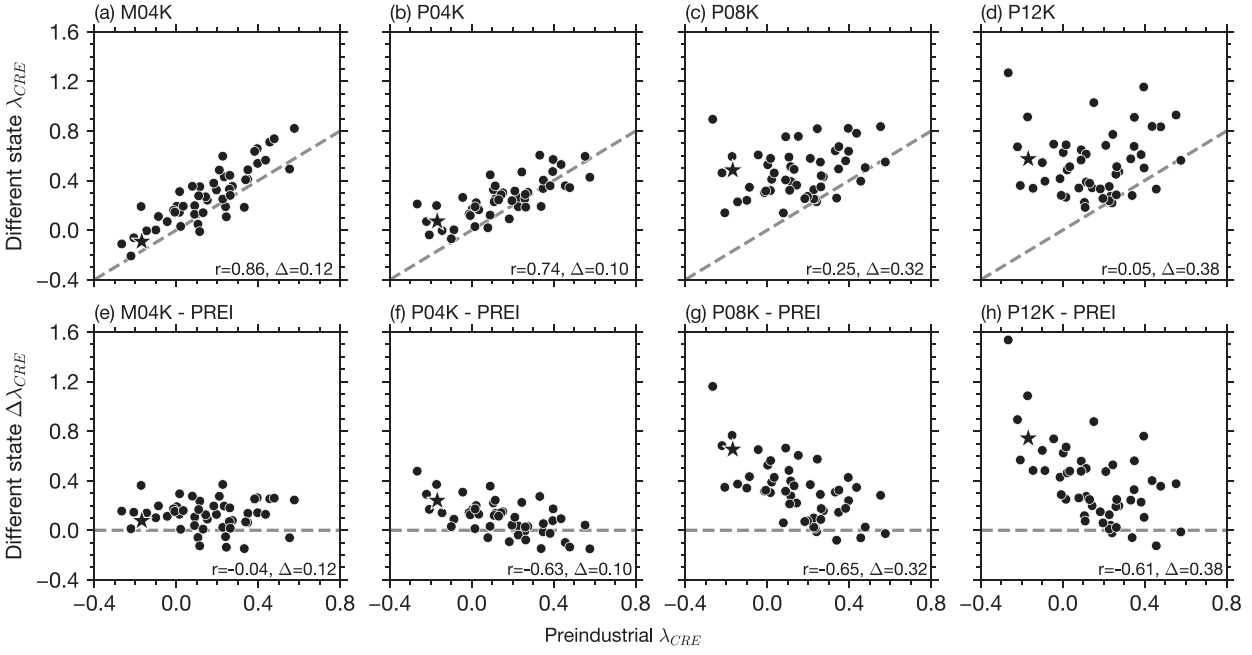

FIG. 5. Comparison of the global mean cloud feedback in PREI (*x* axis) and that in (a) M04K, (b) P04K, (c) P08K, and (d) P12K (*y* axis), as well as the state dependence defined as the cloud feedback change in (e) M04K, (f) P04K, (g) P08K, and (h) P12K from that in PREI (*y* axis). The correlation coefficient and mean difference are listed in each figure. The results are from the top 50 ensemble members. The star denotes the simulation with the default parameters (W m^{-2} K^{-1}).

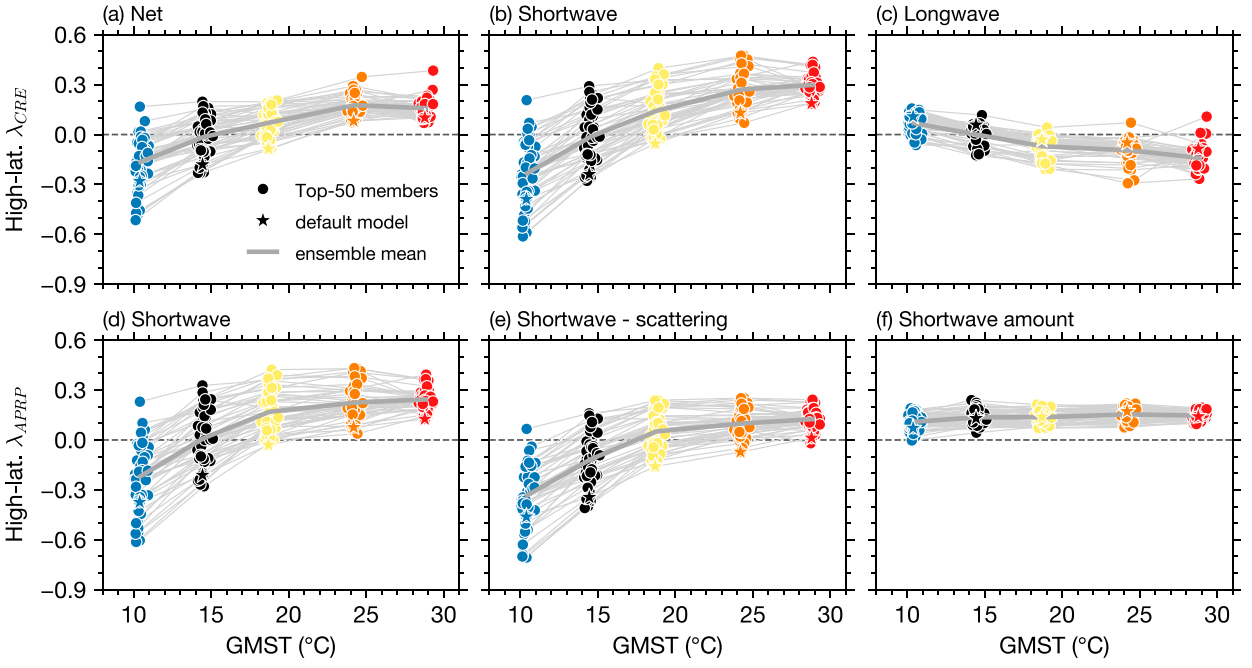

FIG. 6. (a) High-latitude net cloud feedback for the background states with a uniform ΔSST of −4 K (M04K in blue), 0 K (PREI in black), 4 K (P04K in yellow), 8 K (P08K in orange), and 12 K (P12K in red) added to the PREI. Values are weighted by the area coverage and measure their direct contribution to the global mean in Fig. 4a. (b),(c) As in (a), but for the shortwave and longwave components, respectively. (a)–(c) The CRE method λ_{CRE}. (d) As in (b), but with the APRP method λ_{APRP}. (e),(f) As in (d), but for the cloud scattering and amount components, respectively. The results are from the top 50 ensemble members (W m^{-2} K^{-1}).

with the preindustrial value (0.05; Fig. 5d), potentially indicating larger uncertainty in modeling the cloud processes under extreme conditions. In general, the state dependence of the cloud feedback is smaller than the range of the cloud feedback across PPEs.

A clear negative relationship ($r = -0.6$) between preindustrial cloud feedback and its state dependence is identified in the PPEs—i.e., members with stronger preindustrial cloud feedback are associated with smaller increases with warming (Figs. 5e–h). This relationship holds for both high and low latitudes but is more pronounced at high latitudes, with correlation coefficients of −0.9 and −0.5, respectively (figures not shown). As discussed in section 4, this correlation arises likely from processes related to thermodynamic and lower-tropospheric stability. The negative relationship suggests that reducing biases in preindustrial cloud feedback could help constrain uncertainties in its state dependence. Additionally, it may mitigate some risks associated with positive feedback temperature dependence (Bloch-Johnson et al. 2021).

4. Further decomposition and mechanisms for the state dependence

We next investigate mechanisms for the state dependence through the decomposition of the cloud feedback into different components, correlation with large-scale and cloud state variables using the cloud-controlling factor (CCF) framework, and through examining the sensitivity to model parameters. In the CCF framework, λ_{CRE} can be written as

$$\lambda_{\mathrm{CRE}} = \frac{\partial \mathrm{CRE}}{\partial T} = \frac{\partial \mathrm{CRE}}{\partial \mathrm{CCF}} \frac{\partial \mathrm{CCF}}{\partial T}. \tag{3}$$

Note that the CCF framework emphasizes the large-scale environmental changes and the associated impact on CCFs ($\partial \mathrm{CCF}/\partial T$) and assumes that clouds responding to the local values of the cloud-controlling factors ($\partial \mathrm{CRE}/\partial \mathrm{CCF}$) remain largely unchanged (Klein et al. 2017).

a. *High latitudes*

In the PPE simulations, the high-latitude (poleward of 40°N/S) cloud feedback and its state dependence are primarily produced by the shortwave component through processes that impact the cloud optical depth. Figures 6a–c show λ_{CRE} decomposed into shortwave and longwave components. The longwave component is several times smaller in magnitude and plays a secondary role to oppose the shortwave. The ensemble mean of the shortwave increases by 0.50 W m^{-2} K^{-1} from M04K to P08K, with a smaller cancelation of −0.16 in the longwave (scaled values showing the net contribution to the global mean). Interestingly, the increase of cloud feedback with warming saturates in P08K and does not further increase in M12K. The APRP calculation (λ_{APRP}) reproduces the shortwave λ_{CRE} from the CRE method and further decomposes it into contributions from changes in cloud amount and scattering (absorption contribution is small and not shown; Figs. 6d–f). The APRP decomposition suggests that the shortwave cloud feedback and its state dependence are determined by the cloud scattering components (the cloud

optical depth feedback). The contribution from the cloud amount change is approximately 0.14 W m^{-2} K^{-1} and largely invariant with climate change.

Several physical mechanisms could explain the increase and eventual saturation of the cloud optical-depth feedback with warming (Fig. 6e). The cloud optical depth can increase because of the increase of the water path or the decrease in the particle size (Stephens 1978). Accordingly, a warming-induced melt of cloud ice into liquid water increases the cloud optical depth due to the smaller particle size of liquid droplets than ice particles, which forms the cloud-phase feedback to dampen the initial surface warming (Mitchell et al. 1989; Tan et al. 2016). Moreover, the reduction of cloud ice can increase cloud water due to the higher precipitation efficiency (bigger sizes) of ice clouds, forming the cloud-lifetime feedback (Mülmenstädt et al. 2021; Frazer and Ming 2022). Both the cloud-phase and lifetime feedbacks are negative and depend on the cloud ice content in the background climate, which follows simple thermodynamics and can give rise to a weakening and eventual saturation of the feedback as ice in mixed-phase clouds melts and disappears with warming. Nevertheless, the details of the responses of mixed-phase clouds are subject to both parametric and structural uncertainties (Gettelman et al. 2023; Zhao et al. 2023). In addition to the thermodynamic cloud ice mechanism, surface warming can increase the cloud liquid water through a moist adiabatic process, in which cloud condensation along moist adiabats increases with temperature due to the exponential Clapeyron–Clausius relationship (Betts and Harshvardhan 1987). Importantly, a thermodynamic decrease in the moist adiabatic lapse rate with warming means that the warming-induced increase in the cloud water is relatively stronger at lower temperatures, which leads to a state dependence and a potential saturation (Betts and Harshvardhan 1987).

Analysis of the PPEs indicates that the moist adiabatic mechanism, rather than the cloud ice mechanism, is responsible for the high-latitude cloud optical-depth feedback and its state dependence. To demonstrate this, we use the CCF framework to examine the role of cloud liquid water path (LWP) and ice water path (IWP). We focus on the shortwave λ_{CRE} in PREI and the increases from M04K to P08K to maximize the signal in state dependence (Fig. 6b). In response to warming, both magnitudes of $\partial\mathrm{LWP}/\partial T$ and $\partial\mathrm{IWP}/\partial T$ decrease and reach a saturation under high temperatures (Figs. 7a,b), which are quantitatively consistent with both thermodynamical moist adiabatic and cloud ice mechanisms. However, λ_{CRE} in PREI correlates much stronger with $\partial\mathrm{LWP}/\partial T$ ($r = -0.8$) than with $\partial\mathrm{IWP}/\partial T$ ($r = -0.3$) among the top 50 PPE members (Figs. 7c,d). Similarly, $\Delta\lambda_{\mathrm{CRE}}$ (calculated as the difference between P08K and M04K) correlates much stronger with $\Delta(\partial\mathrm{LWP}/\partial T)$ than with $\Delta(\partial\mathrm{IWP}/\partial T)$, with correlation coefficients of −0.8 and 0.0, respectively (Figs. 7e,f). The correlation analysis suggests a predominant role of the moist adiabatic mechanisms in determining the high-latitude cloud optical depth feedback and its state dependence. Additionally, no correlation is found between the background IWP and the warming-induced ΔLWP in PREI, indicating that the increase in LWP is not due to the melt of cloud ice. The correlation does not depend on whether we rank the PPEs or not (not shown), consistent with the simple and robust thermodynamic mechanism that are insensitive to model parameters.

Our mechanistic explanation is supported by the parameter sensitivity in the PPE simulations. Figure 8 shows the linear regression coefficients of the shortwave cloud feedback and its state dependence against model parameters. Model parameters are normalized (scaled to be between 0 and 1 by the minimum and maximum parameter values), and cloud feedbacks are standardized (scaled to have a mean of 0 and a standard deviation of 1) before the regression analysis. In general, the high-latitude λ_{CRE} is mostly sensitive to the microphysical parameters related to liquid water (left column of Fig. 8), e.g., the liquid water content exponential coefficient (micro_mg_autocon_lwp_exp) in the autoconversion formula and the accretion enhancement factor (micro_mg_accre_enhanc_factor). Similarly, the increase of λ_{CRE} with warming ($\Delta\lambda_{\mathrm{P08K-M04K}}$) is also mostly influenced by the two microphysical parameters. A higher micro_mg_autocon_lwp_exp decreases the cloud liquid-to-rain autoconversion rate (note that the in-cloud liquid water content is smaller than 1 Kg Kg^{-1}) and increases the LWP in the model. As a result, this configuration will allow more increase of the LWP with warming, leading to more negative cloud feedback. The state dependence ($\Delta\lambda_{\mathrm{CRE}}$) becomes greater due to the greater potential to reach cloud feedback saturation. We note that these cloud microphysical parameters control the sink of cloud water and could increase as a nonlinear function of the cloud liquid water content. For example, in the commonly used scheme (Khairoutdinov and Kogan 2000), both the autoconversion and accretion rates increase exponentially with cloud water content. Therefore, the saturation of λ_{CRE} with warming potentially represents a combination of the thermodynamic weakening of LWP increase and a microphysical increase of sinks of cloud water.

In sum, model configurations that allow more LWP in the background climate show more LWP increase due to warming (see also Gettelman et al. 2024), thus more negative cloud feedback (the so-called liquid water lapse-rate feedback). Due to nonlinearities rooted in relatively simple thermodynamics (and potentially microphysics), the cloud feedback could saturate with warming, which means that a model configuration with more negative cloud feedback in the present climate will feature more increases with warming in the future. Other mechanisms, such as the changes in cloud phase, particle size, entrainment drying, and moisture convergence from lower latitudes, could be secondary (McCoy et al. 2023, 2022). Notably, we found no correlation between moisture convergence and the high-latitude cloud feedback across PPE members (not shown). We suggest that the potential state dependence from the autoconversion and accretion formula should be further studied. Our findings also indicate that targeted improvements or emergent constraints on present-day LWP could help refine and better constrain high-latitude cloud feedback and its state dependence.

b. *Low latitudes*

The state dependence of the low-latitude cloud feedback is nonmonotonic and more complicated than that in high latitudes.

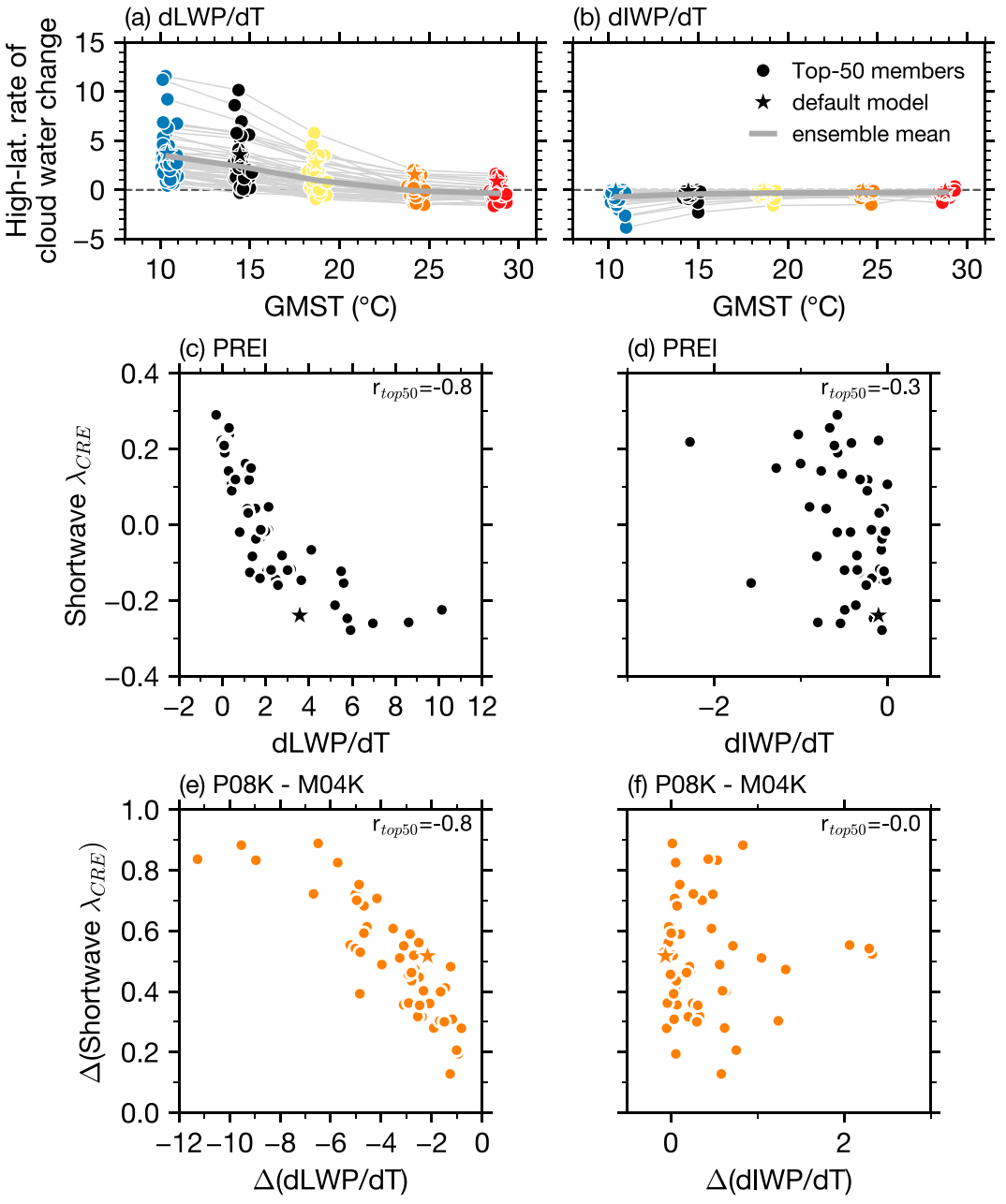

FIG. 7. Rate of cloud (a) LWP and (b) IWP changes with warming (g kg^{-1} K^{-1}) over the high latitude for the background states with uniform ΔSST of −4 K (M04K in blue), 0 K (PREI in black), 4 K (P04K in yellow), 8 K (P08K in orange), and 12 K (P12K in red) added to PREI. Scatterplot of the shortwave cloud feedback (λ_{CRE}; W m^{-2} K^{-1}) against the rate of cloud (c) LWP and (d) IWP changes with warming under the PREI condition. The scatterplot of the changes in the shortwave cloud feedback between P08K and M04K ($\Delta\lambda_{CRE}$) against the corresponding variation in the rate of cloud (e) LWP and (f) IWP changes with warming. Correlation coefficients are listed in (c)–(f). The results are from the top 50 ensemble members.

The ensemble mean λ_{CRE} decreases by 0.27 W m^{-2} K^{-1} from M04K to PREI and then increases gradually by 0.21 W m^{-2} K^{-1} in P12K (Fig. 9a; scaled values showing the net contribution to the global mean). The λ_{CRE} over the ocean plays a dominant role while the feedback over land has a smaller positive contribution that weakens gradually with warming (Figs. 9b,c). We focus on the marine low-latitude feedback and further decompose it into that from the subsidence and ascent regimes using 500-hPa vertical pressure velocity as a criterion (ω500; Bony et al. 2004). Over both the ascent and subsidence regions, the shortwave λ_{CRE} first decreases from M04K to P04K and then increases slightly afterward with an overall larger contribution from

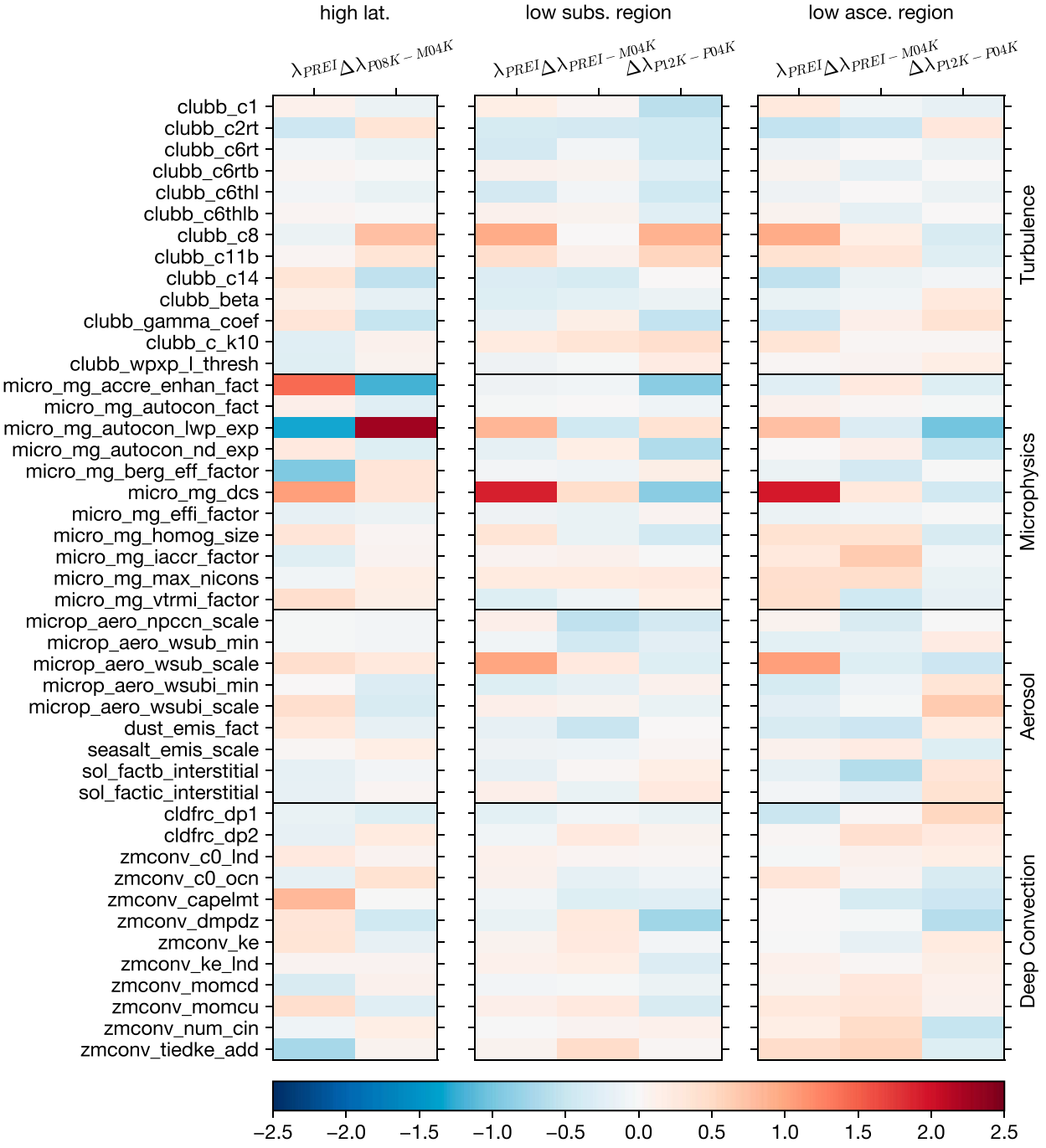

FIG. 8. Slopes of the linear regression of the shortwave cloud feedback and state dependence (x axis) against model parameters (y axis) over the (left) high-latitude, (middle) low-latitude subsidence, and (right) ascent regions. Regression is performed for the PREI cloud feedback (λ_{PREI}) and the changes between P08K and M04K ($\Delta\lambda_{P08K-M04K}$) over the high latitude, and between PREI and M04K ($\Delta\lambda_{PREI-M04K}$) and between P12K and P04K ($\Delta\lambda_{P12K-P04K}$) over the low latitude. Model parameters are normalized, and cloud feedbacks are standardized before the regression analysis. Model parameters are grouped into turbulence and shallow convection, microphysics, aerosol, and deep convection. For more robust statistics, all ensemble members are used in the analysis.

the subsidence region. APRP analysis suggests that both the cloud amount and scattering components contribute to the total shortwave feedback (not shown). The longwave λ_{CRE} over both regions increases with warming from M04K to P04K, partly canceling the decreases in the shortwave. We note that these cloud feedback changes are not attributable to the relatively small area changes (<3%) in the ascent and subsidence regions; they are consistent across low latitudes (see also Fig. 4b).

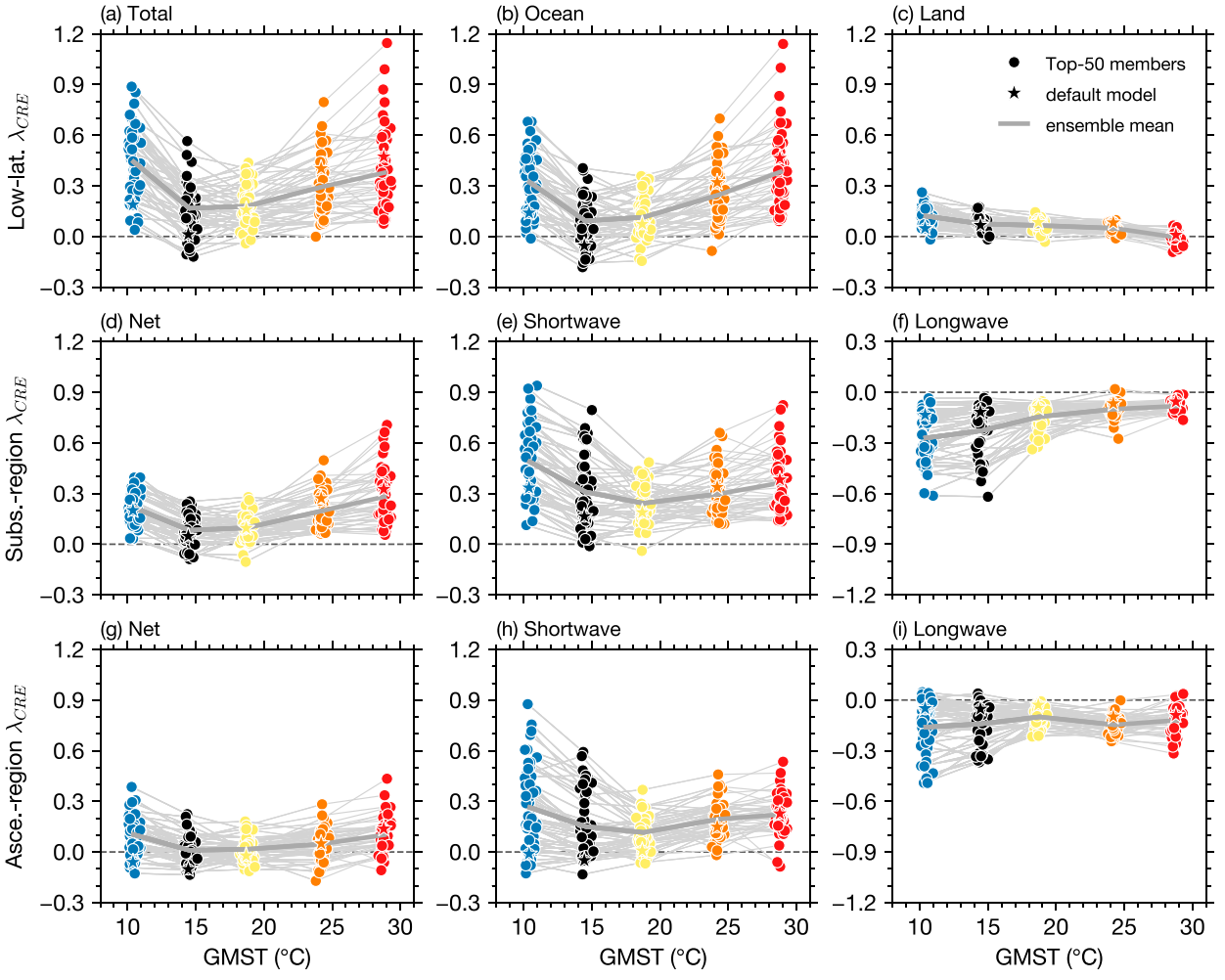

FIG. 9. (a) Low-latitude total cloud feedback (W m^{-2} K^{-1}) for the background states with uniform ΔSST of −4 K (M04K in blue), 0 K (PREI in black), 4 K (P04K in yellow), 8 K (P08K in orange), and 12 K (P12K in red) added to PREI. (b),(c) As in (a), but for the decomposition into values over ocean and land, respectively. (d) The net cloud feedback over the low-latitude subsidence region according to the vertical velocity at 500 hPa and its (e) shortwave and (f) longwave components. (g)–(i) As in (d)–(f), but for the cloud feedback over the low-latitude ascent region. The CRE method (λ_{CRE}) is used in the calculation. The λ_{CRE} values are weighted by the area coverage and measure their direct contribution to the global mean in Fig. 4a. The results are from the top 50 ensemble members.

We use the CCF framework to examine the potential contribution of multiple processes on the cloud feedback and its state dependence over both the ascent and subsidence regions (Qu et al. 2015b; Klein et al. 2017; Scott et al. 2020). For low latitudes, we investigate CCFs including the estimated inversion strength (EIS) as an indicator for the lower-tropospheric stability (Wood and Bretherton 2006), ω500 for the large-scale circulation (Myers and Norris 2013), the specific humidity difference between 700 hPa and surface dQ as an indicator for the inversion specific humidity gradient (Brient and Bony 2013), and the surface latent heat flux (LHF) for vertical mixing by boundary layer turbulence or convection (Rieck et al. 2012). Our choice of CCFs differs from previous studies mainly in that we do not use SST or SST advection because it is prescribed and invariant among our ensemble members. Briefly, a larger dEIS/dT [see Eq. (3)] strengthens more the lower-tropospheric stability and promotes more increase in low clouds with warming. A larger $d\omega500/dT$ means less weakening of large-scale subsidence and produces less increase in low clouds. A larger dLHF/dT means more energy to increase vertical mixing by turbulence or convection, which desiccates more low clouds. A larger dQ/dT leads to more entrainment drying on low clouds. We refer readers to published work (Klein et al. 2017; Bretherton 2015; Scott et al. 2020; Webb et al. 2024) for further discussion on relevant physical processes.

Consistent with previous work (Qu et al. 2015b; Klein et al. 2017; Scott et al. 2020), the preindustrial λ_{CRE} in our PPEs can be well explained using these CCFs. Over the subsidence regions, EIS, ω500, and LHF are found to be the most influential CCFs, while EIS and LHF are dominant over the ascent regions. Together, a multiple linear regression model has a good skill reproducing the preindustrial λ_{CRE} in both the subsidence and ascent regions and can explain more than 70% of the total variance with a mean absolute error less than 0.1 W m^{-2} K^{-1}

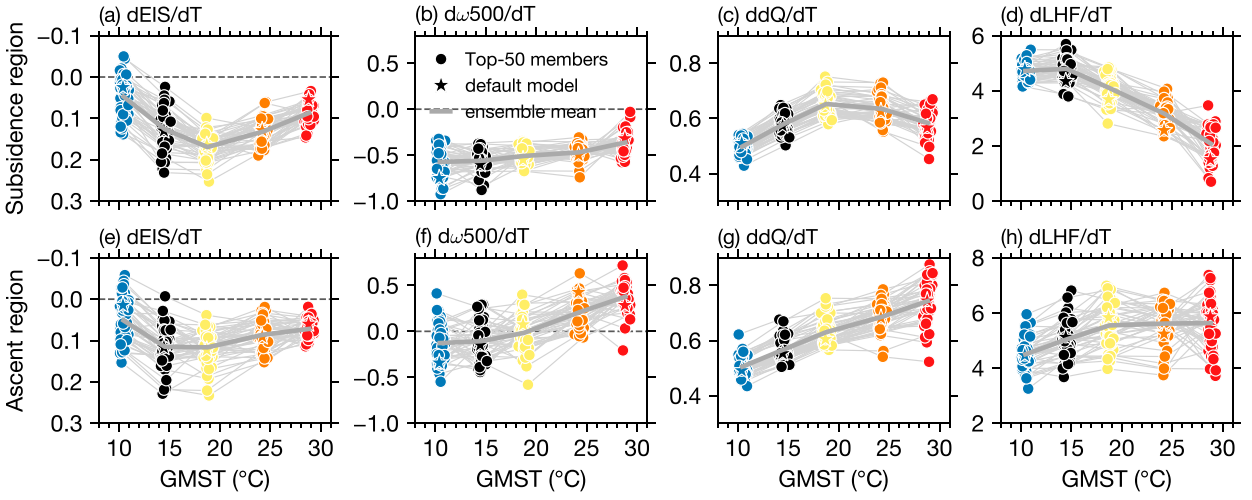

FIG. 10. (a) Rate of changes in the mean EIS with warming (K K^{-1}) over the low-latitude subsidence region for the background states with a uniform ΔSST of −4 K (M04K in blue), 0 K (PREI in black), 4 K (P04K in yellow), 8 K (P08K in orange), and 12 K (P12K in red) added to PREI. (b)–(d) As in (a), but for the vertical velocity at 500 hPa ω500 (hPa day^{-1} K^{-1}), the specific humidity contrast between surface and 700 hPa dQ (g kg^{-1} K^{-1}), and the LHF (W m^{-2} K^{-1}), respectively. (e)–(h) As in (a)–(d), but for these CCFs over the low-latitude ascent region. The results are from the top 50 ensemble members.

(not shown; similar results from Ridge and Lasso regression models).

State dependence of EIS resembles most closely the state dependence of low-latitude cloud feedback. Figure 10 shows the variations in the mean CCFs with GMST over the subsidence and ascent regions, which are plotted such that upward means CCFs contribute to stronger cloud feedbacks. In response to a uniform 4-K warming in PREI, EIS increases at a rate of ~0.1 K K^{-1} over low latitudes (Figs. 10a,e), which is comparable to values in CMIP models (Qu et al. 2015a). The dEIS/dT is not constant and increases with warming from M04K to P04K and then decreases to values less than 0.1 K K^{-1} in P12K (note the reversed y axis). All else being equal, the evolution of dEIS/dT would produce cloud feedback that first decreases and then increases with warming, which is what we observe in Figs. 9d and 9g. The importance of dEIS/dT is confirmed by its relatively high correlation with λ_{CRE} in PREI and its state dependence including the decrease from P04K to M04K and the increase from P04K to P12K ($r = -0.6$, -0.3, and -0.4, respectively).

We suggest that the variation of dEIS/dT with GMST could be due to the competing effects from the nonlinearity in thermodynamics and changes in the large-scale circulation. We note that an overall positive dEIS/dT has been attributed to a known thermodynamic mechanism. In this mechanism, the enhanced warming with height due to tropical moist convection and latent heating is propagated into the subtropics via tropical waves and the mean overturning circulation, increasing the lower-tropospheric stability (dEIS/$dT > 0$) (Qu et al. 2015a; Webb et al. 2018). Our focus here is on the state dependence of dEIS/dT. In our PPEs, the ensemble mean of dLHF/dT over the ascent region increases with the warming from M04K to P04K and flattens with further warming (Fig. 10h), which contributes to an increase of dEIS/dT that saturates at P04K. At the same time, a continued weakening of the tropical subsidence ($d\omega500/dT$ in Fig. 10b) is a robust response to warming according to theory and modeling (Vecchi and Soden 2007; Held and Soden 2006) and could contribute to a weaker inversion change (dEIS/dT) following the relationship seen in observations (Myers and Norris 2013). We hypothesize that the thermodynamics-driven increasing (dLHF/dT) and the dynamics-driven decreasing ($d\omega500/dT$) effects compete and produce a U-shaped dEIS/dT. We further suggest that the increase of dLHF/dT over the ascent region is due to the exponential Clapeyron–Clausius relationship, while the flattening after P04K could be due to the weakening of surface winds and a thermodynamics-induced increase of the near-surface relative humidity with warming [e.g., Richter and Xie 2008; Eq. (3) of Schneider et al. (2010)].

In contrast to EIS, the other CCFs (ω500, dQ, and LHF) do not resemble as well the overall evolution of the cloud feedback with warming. However, the tropical LHF and ω500 may indirectly influence the cloud feedback through changing EIS (see the discussion above). In addition, the rate of circulation weakening ($d\omega500/dT$) becomes smaller in magnitude for very warm climates (Fig. 10b), which could directly strengthen the cloud feedback with warming from P04K to P12K. Over the subsidence region, dQ/dT in general first increases and then decreases with warming, which is opposite to the state dependence of the cloud feedback. However, dQ/dT over the ascent region increases with warming consistently, which may contribute to the increase of the cloud feedback from P04K to P12K through enhancing the entrainment drying of low clouds.

We next explore the sensitivity of the low-latitude cloud feedback to model parameters. The low-latitude cloud feedback in PREI is primarily influenced by the microphysical ice–snow autoconversion parameter (micro_mg_dcs; first

column of the middle and right panels of Fig. 8). A higher micro_mg_dcs reduces ice–snow autoconversion (microphysical snow formation) and increases cloud IWP, LWP, and cloud cover in the background climate, likely due to an overall lower precipitation efficiency. In response to warming, PPEs with higher micro_mg_dcs simulate a greater reduction in cloud condensates and cover, and thus a stronger cloud feedback [see also Fig. 10 of Gettelman et al. (2024)]. This relationship between the cloud feedback and the background clouds can be explained by the so-called "beta feedback" (Brient and Bony 2012): A low-cloud reduction decreases the cloud-top radiative cooling and relative humidity in the BL, which amplifies the low-cloud reduction, forming a feedback loop with its strength depending on the background clouds. Additionally, micro_mg_dcs also acts in the tropics, suggesting an additional role of the tropical cirrus clouds [Figs. 9 and 11 of Gettelman et al. (2024)]. More discussion on the sensitivity to model parameters can be found in Gettelman et al. (2024). In contrast to the mean state cloud feedback, the state dependence (e.g., $\Delta\lambda$ between P04K and M04K, and between P12K and P04K; Fig. 8) appears to rely less on individual cloud parameters, which is consistent with our explanations (see above) related to large-scale stability, circulation, and their connections to simple nonlinear thermodynamics.

In summary, the state dependence of low-latitude cloud feedback primarily arises from the shortwave component over the ocean. This feedback shows a strong correlation with the state dependence of the estimated inversion strength, which we hypothesize is due to nonlinearity in thermodynamics and large-scale circulation. To further investigate this relationship, mechanism-denial experiments are needed, such as simulations with fixed circulation. This will be the focus of our future research.

5. Discussion and conclusions

a. *Discussion*

Our investigation of the cloud feedback with a variety of parameter configurations over a wide range of global temperatures represents an effective way to identify robust cloud feedback processes. Specifically, the important role of the cloud liquid water on the high-latitude cloud feedback emphasizes the moist adiabatic mechanism (Betts and Harshvardhan 1987; Mülmenstädt et al. 2021; Frazer and Ming 2022) over the debated cloud ice mechanisms in mixed-phase clouds (e.g., Tan et al. 2016). The significant influence of cloud microphysical parameters, particularly those regarding liquid water autoconversion and accretion, points to the necessity for further research to reduce uncertainties in these areas. Additionally, the good match of the lower-tropospheric stability change with the low-latitude cloud feedback across different climate states emphasizes the vital connection between the atmospheric stability and cloud processes. Future studies should aim to deepen our understanding of stability changes and their interactions with dynamical, thermodynamical, and radiative processes, ultimately enhancing our comprehension of cloud feedback mechanisms and refining climate model predictions. Future work with different models/parameterizations is needed to test the sensitivity to model structural uncertainties, which are challenging to explore in a single model with known structural biases in mixed-phase clouds and warm rain processes (Gettelman et al. 2020; Medeiros et al. 2023; Gettelman et al. 2021).

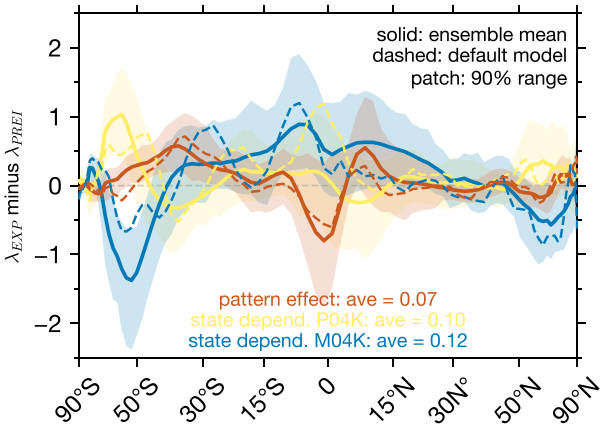

FIG. 11. Comparison of the state dependence and the SST pattern effect of the cloud feedback. State dependence is the cloud feedback change from PREI for the background states with uniform 4-K SST cooling ($\lambda_{\mathrm{M04K}-}\lambda_{\mathrm{PREI}}$ in blue) and warming ($\lambda_{\mathrm{P04K}-}\lambda_{\mathrm{PREI}}$ in yellow). The pattern effect is the cloud feedback change from PREI for the experiment with a patterned 4-K SST warming from PREI ($\lambda_{\mathrm{PREI\_P04K\_PAT}-}\lambda_{\mathrm{PREI}}$ in brown). The results are from the top 50 ensemble members (W m^{-2} K^{-1}).

Our results suggest that state dependence of the cloud feedback could be as important as the SST pattern effect within a typical ΔGMST range of an abrupt 4×CO_2 simulation of 150 years. Figure 11 compares the zonal mean cloud feedback changes resulting from the state dependence (blue for M04K and yellow for P04K) and the SST pattern effect (brown for PREI_PAT). The pattern effect is calculated as the cloud feedback difference between P04K_PAT and P04K, both with PREI as a reference. The SST pattern in P04K_PAT is derived from the fully coupled 4×CO_2 simulation (averaged between years 131 and 150). The global mean $\Delta\lambda_{\mathrm{CRE}}$ associated with state dependence is slightly larger than that from the pattern effect (0.10 and 0.12 vs 0.07 W m^{-2} K^{-1}). The larger state dependence is more prominent at regional scales. From these results, we suggest that the state dependence from a 4-K warming or cooling could be as important as, if not more important than, the SST pattern effect, although the results may depend on the details of the SST pattern. We further suggest that mechanistic understanding and quantification of the cloud feedback should be carefully performed with considerations of both the state dependence and pattern effect.

Stronger low-latitude cloud feedback under conditions colder than the preindustrial has been found in simulations of the Last Glacial Maximum using multiple generations of CESM (Zhu and Poulsen 2021; Zhu et al. 2021). Likewise, stronger global cloud feedback is consistently observed in simulations of warmer conditions (Caballero and Huber 2013; Zhu et al. 2019; Zhu and Poulsen 2020). Here, we find that uniform cooling or warming can lead to significantly enhanced cloud feedback. This nonlinear state dependence is tied to fundamental

thermodynamic mechanisms, specifically the moist adiabatic processes involving cloud liquid water at high latitudes and the tropical latent heating that influences the lower-tropospheric stability at low latitudes. Changes in the tropical circulation may also contribute additional mechanisms. However, we recognize that using cloud-controlling factors may limit our ability to identify causality between cloud processes and their environments. To address this, future studies should employ mechanism-denial simulations—where circulation or clouds are fixed—to disentangle the complex interactions among circulation, thermodynamics, and lower-tropospheric stability. This will be a focus of our future research.

Nevertheless, integrating state dependence and the pattern effect into paleoclimate constraints on climate sensitivity is crucial. The research by Cooper et al. (2024) is pivotal in this regard, as it provides a comprehensive framework that incorporates both the pattern effect and state dependence in cloud feedback, along with other climate feedbacks. Particularly for distant periods in Earth's history like the early Eocene (~50 million years ago with a GMST of ~14°C warmer), where conditions were markedly different from today's climate, understanding state dependence becomes increasingly important (Zhu et al. 2024, 2019).

b. Conclusions

In this study, we performed a suite of PPE simulations to investigate the state dependence of the cloud feedback over a wide range of global mean surface temperatures that covers roughly the past 66 million years. Multiple sets of PPE simulations were run employing an updated version of CAM6 in the preindustrial condition with prescribed uniform SST perturbations of −4, 0, +4, +8, +12, and +16 K. Each PPE set uses 250 ensemble members to sample uncertainty of 45 parameters in cloud microphysics, aerosol, convection and turbulence. After removing configurations that are less realistic according to satellite observations and expert assessments, the top 50 PPE members still exhibit wide ranges in cloud properties and feedbacks comparable to those in CMIP5 and CMIP6 models, supporting PPE as an effective approach for exploring model uncertainties within a single-model framework. We contend that our PPE approach with a wide temperature range could provide more robust results on the state dependence than previous studies that rely on a single model or configuration (Caballero and Huber 2013; Zhu et al. 2019; Zhu and Poulsen 2020).

Our results suggest a nonconstant cloud feedback parameter that increases to higher values under both colder and warmer GMSTs. Under a climate colder by ~4 K than the preindustrial (M04K), the global mean cloud feedback increases by 0.12 ± 0.12 W m^{-2} K^{-1} (one standard deviation derived from the top 50 members) from the preindustrial with 44 of the top 50 members exhibiting an increase. Under conditions warmer than the preindustrial, the cloud feedback strengthens gradually with GMST with an increase of 0.38 ± 0.32 W m^{-2} K^{-1} in the warmest state (P12K), with 46 out of the top 50 members showing an increasing trend. The state dependence of cloud feedback results from distinct behaviors over the high and low latitudes (divided broadly by 40°N/S) and are linked to the large-scale changes in thermodynamics and circulation.

Over high latitudes, the cloud feedback increases monotonically by 0.34 ± 0.16 W m^{-2} K^{-1} from M04K to P08K and appears to reach saturation in P08K (scaled values showing the net contribution to the global mean). This response correlates strongly with changes in cloud liquid water, which suggests a moist adiabatic mechanism, i.e., the cloud liquid water feedback (Betts and Harshvardhan 1987). In this thermodynamic mechanism, the rate of warming-induced increase in cloud water scales with the change in the moist adiabatic lapse rate rather than the changes in the saturation mixing ratio. As a result, the rate of cloud water increase is relatively higher at lower temperatures, giving rise to the temperature dependence and eventual saturation of the cloud liquid water feedback. In contrast, the feedbacks related to the cloud ice content, such as cloud lifetime and phase changes in mixed-phase clouds, appear to have a secondary influence. This is supported by the very weak or negligible correlation between cloud feedback and variations in the cloud ice water content. Moreover, the strong correlation of high-latitude cloud feedback with microphysical parameters related to cloud liquid water processes—such as autoconversion and accretion—further underscores the dominant influence of the cloud liquid water feedback and the moist adiabatic mechanism.

Over low latitudes, the cloud feedback increases under both colder and warmer conditions compared to the preindustrial, showing an increase of 0.27 ± 0.12 W m^{-2} K^{-1} in a 4-K colder climate (M04K) and a gradual increase of 0.21 ± 0.26 W m^{-2} K^{-1} in a 12-K warmer climate. The state dependence is primarily driven by the cloud feedback over the ocean, with a greater contribution from subsidence than from ascent regions. Using the framework of cloud-controlling factor, the state dependence is found to follow most closely the EIS variations, suggesting an important role of the lower-tropospheric stability in regulating the cloud behavior. The variations in EIS sensitivity, the initial increase in $d\text{EIS}/dT$ from M04K to PREI and the subsequent decrease to P12K, are hypothesized to result from competing effects from the nonlinearity in thermodynamics and changes in the large-scale circulation. The rate of latent heat increase with warming ($d\text{LHF}/dT$) over the tropical ascent region strengthens from M04K to P04K and becomes saturated afterward, which could contribute to the initial increasing $d\text{EIS}/dT$ through affecting the free troposphere temperature via latent heating (Webb et al. 2018). This nonlinearity in the latent heat sensitivity, in turn, could result from combined effects of the exponential Clapeyron–Clausius relationship (e.g., Schneider et al. 2010) and the declining surface winds and increasing near-surface relative humidity with warming (e.g., Richter and Xie 2008). In addition, the weakening of tropical circulations emerges as a consistent response to warming, which could impact the cloud feedback either indirectly through regulating the EIS or directly through impacting the cloud-top entrainment (Myers and Norris 2013), which, we suggest, may be important for the decrease in $d\text{EIS}/dT$ and the increase in cloud feedback after P04K. This intricate interplay between thermodynamics and circulation

emphasizes the complex dynamics of cloud feedback processes in low-latitude regions.

Acknowledgments. We thank two anonymous reviewers for their helpful comments that improved the manuscript. The CESM project is supported primarily by the National Science Foundation (NSF). This material is based upon work supported by the National Center for Atmospheric Research (NCAR), which is a major facility sponsored by the NSF under Cooperative Agreement 1852977. We would like to acknowledge high-performance computing support from the Cheyenne (https://doi.org/10.5065/D6RX99HX) and Derecho (https://doi.org/10.5065/qx9a-pg09) systems provided by the NSF NCAR, sponsored by the NSF. This work was supported by NSF Grants 2303567 and 2202777 to J. Z., and 2303566 to R. F. The Pacific Northwest National Laboratory is operated for the U.S. Department of Energy by the Battelle Memorial Institute under contract DE-AC05-76RL01830.

Data availability statement. The PPE dataset and the CESM2 CAM code version cam6_3_026 (including the paleoclimate fixes) are available at the NSF NCAR Research Data Archive (https://doi.org/10.5065/6AQH-6S22). The ISCCP cloud fraction data are available at https://doi.org/10.7289/V5QZ281S. The CERES EBAF Ed4.2 data on the cloud radiative effects can be visualized, subsetted, and ordered at https://ceres.larc.nasa.gov/data/.

REFERENCES

Abbot, D. S., and E. Tziperman, 2008: A high-latitude convective cloud feedback and equable climates. *Quart. J. Roy. Meteor. Soc.*, **134**, 165–185, https://doi.org/10.1002/qj.211.

Andrews, T., and M. J. Webb, 2018: The dependence of global cloud and lapse rate feedbacks on the spatial structure of tropical Pacific warming. *J. Climate*, **31**, 641–654, https://doi.org/10.1175/JCLI-D-17-0087.1.

Armour, K. C., C. M. Bitz, and G. H. Roe, 2013: Time-varying climate sensitivity from regional feedbacks. *J. Climate*, **26**, 4518–4534, https://doi.org/10.1175/JCLI-D-12-00544.1.

——, and Coauthors, 2024: Sea-surface temperature pattern effects have slowed global warming and biased warming-based constraints on climate sensitivity. *Proc. Natl. Acad. Sci. USA*, **121**, e2312093121, https://doi.org/10.1073/pnas.2312093121.

Betts, A. K., and Harshvardhan, 1987: Thermodynamic constraint on the cloud liquid water feedback in climate models. *J. Geophys. Res.*, **92**, 8483–8485, https://doi.org/10.1029/JD092iD07p08483.

Bloch-Johnson, J., M. Rugenstein, M. B. Stolpe, T. Rohrschneider, Y. Zheng, and J. M. Gregory, 2021: Climate sensitivity increases under higher CO_2 levels due to feedback temperature dependence. *Geophys. Res. Lett.*, **48**, e2020GL089074, https://doi.org/10.1029/2020GL089074.

Bock, L., and A. Lauer, 2024: Cloud properties and their projected changes in CMIP models with low to high climate sensitivity. *Atmos. Chem. Phys.*, **24**, 1587–1605, https://doi.org/10.5194/acp-24-1587-2024.

Bodas-Salcedo, A., and Coauthors, 2011: COSP: Satellite simulation software for model assessment. *Bull. Amer. Meteor. Soc.*, **92**, 1023–1043, https://doi.org/10.1175/2011BAMS2856.1.

Bogenschutz, P. A., A. Gettelman, H. Morrison, V. E. Larson, C. Craig, and D. P. Schanen, 2013: Higher-order turbulence closure and its impact on climate simulations in the community atmosphere model. *J. Climate*, **26**, 9655–9676, https://doi.org/10.1175/JCLI-D-13-00075.1.

Bony, S., J.-L. Dufresne, H. Le Treut, J.-J. Morcrette, and C. Senior, 2004: On dynamic and thermodynamic components of cloud changes. *Climate Dyn.*, **22**, 71–86, https://doi.org/10.1007/s00382-003-0369-6.

Bretherton, C. S., 2015: Insights into low-latitude cloud feedbacks from high-resolution models. *Philos. Trans. Roy. Soc.*, **A373**, 20140415, https://doi.org/10.1098/rsta.2014.0415.

Brient, F., and S. Bony, 2012: How may low-cloud radiative properties simulated in the current climate influence low-cloud feedbacks under global warming? *Geophys. Res. Lett.*, **39**, L20807, https://doi.org/10.1029/2012GL053265.

——, and ——, 2013: Interpretation of the positive low-cloud feedback predicted by a climate model under global warming. *Climate Dyn.*, **40**, 2415–2431, https://doi.org/10.1007/s00382-011-1279-7.

Caballero, R., and M. Huber, 2013: State-dependent climate sensitivity in past warm climates and its implications for future climate projections. *Proc. Natl. Acad. Sci. USA*, **110**, 14 162–14 167, https://doi.org/10.1073/pnas.1303365110.

Caldwell, P. M., M. D. Zelinka, K. E. Taylor, and K. Marvel, 2016: Quantifying the sources of intermodel spread in equilibrium climate sensitivity. *J. Climate*, **29**, 513–524, https://doi.org/10.1175/JCLI-D-15-0352.1.

Ceppi, P., F. Brient, M. D. Zelinka, and D. L. Hartmann, 2017: Cloud feedback mechanisms and their representation in global climate models. *Wiley Interdiscip. Rev.: Climate Change*, **8**, e465, https://doi.org/10.1002/wcc.465.

Cooper, V. T., and Coauthors, 2024: Last glacial maximum pattern effects reduce climate sensitivity estimates. *Sci. Adv.*, **10**, eadk9461, https://doi.org/10.1126/sciadv.adk9461.

Danabasoglu, G., and Coauthors, 2020: The Community Earth System Model version 2 (CESM2). *J. Adv. Model. Earth Syst.*, **12**, e2019MS001916, https://doi.org/10.1029/2019MS001916.

Dong, Y., C. Proistosescu, K. C. Armour, and D. S. Battisti, 2019: Attributing historical and future evolution of radiative feedbacks to regional warming patterns using a Green's function approach: The preeminence of the western Pacific. *J. Climate*, **32**, 5471–5491, https://doi.org/10.1175/JCLI-D-18-0843.1.

Duffy, M. L., B. Medeiros, A. Gettelman, and T. Eidhammer, 2024: Perturbing parameters to understand cloud contributions to climate change. *J. Climate*, **37**, 213–227, https://doi.org/10.1175/JCLI-D-23-0250.1.

Eidhammer, T., and Coauthors, 2024: An extensible perturbed parameter ensemble for the Community Atmosphere Model version 6. *Geosci. Model Dev.*, **17**, 7835–7853, https://doi.org/10.5194/gmd-17-7835-2024.

Frazer, M. E., and Y. Ming, 2022: Understanding the extratropical liquid water path feedback in mixed-phase clouds with an idealized global climate model. *J. Climate*, **35**, 2391–2406, https://doi.org/10.1175/JCLI-D-21-0334.1.

Gettelman, A., and S. C. Sherwood, 2016: Processes responsible for cloud feedback. *Curr. Climate Change Rep.*, **2**, 179–189, https://doi.org/10.1007/s40641-016-0052-8.

——, H. Morrison, S. Santos, P. Bogenschutz, and P. M. Caldwell, 2015: Advanced two-moment bulk microphysics for global models. Part II: Global model solutions and aerosol–cloud

interactions. *J. Climate*, **28**, 1288–1307, https://doi.org/10.1175/JCLI-D-14-00103.1.

——, and Coauthors, 2019: High climate sensitivity in the Community Earth System Model version 2 (CESM2). *Geophys. Res. Lett.*, **46**, 8329–8337, https://doi.org/10.1029/2019GL083978.

——, and Coauthors, 2020: Simulating observations of southern ocean clouds and implications for climate. *J. Geophys. Res. Atmos.*, **125**, e2020JD032619, https://doi.org/10.1029/2020JD032619.

——, D. J. Gagne, C.-C. Chen, M. W. Christensen, Z. J. Lebo, H. Morrison, and G. Gantos, 2021: Machine learning the warm rain process. *J. Adv. Model. Earth Syst.*, **13**, e2020MS002268, https://doi.org/10.1029/2020MS002268.

——, and Coauthors, 2023: Importance of ice nucleation and precipitation on climate with the Parameterization of Unified Microphysics Across Scales version 1 (PUMASv1). *Geosci. Model Dev.*, **16**, 1735–1754, https://doi.org/10.5194/gmd-16-1735-2023.

——, T. Eidhammer, M. L. Duffy, D. T. McCoy, C. Song, and D. Watson-Parris, 2024: The interaction between climate forcing and feedbacks. *J. Geophys. Res. Atmos.*, **129**, e2024JD040857, https://doi.org/10.1029/2024JD040857.

Hansen, J., M. Sato, G. Russell, P. Kharecha, H. James, S. Makiko, R. Gary, and K. Pushker, 2013: Climate sensitivity, sea level and atmospheric carbon dioxide. *Philos. Trans. Roy. Soc.*, **A371**, 20120294, https://doi.org/10.1098/rsta.2012.0294.

Held, I. M., and B. J. Soden, 2006: Robust responses of the hydrological cycle to global warming. *J. Climate*, **19**, 5686–5699, https://doi.org/10.1175/JCLI3990.1.

Henry, M., and G. K. Vallis, 2022: Variations on a pathway to an early Eocene climate. *Paleoceanogr. Paleoclimatol.*, **37**, e2021PA004375, https://doi.org/10.1029/2021PA004375.

Hoose, C., J. E. Kristjánsson, J.-P. Chen, and A. Hazra, 2010: A classical-theory-based parameterization of heterogeneous ice nucleation by mineral dust, soot, and biological particles in a global climate model. *J. Atmos. Sci.*, **67**, 2483–2503, https://doi.org/10.1175/2010JAS3425.1.

Hurrell, J. W., J. J. Hack, D. Shea, J. M. Caron, and J. Rosinski, 2008: A new sea surface temperature and sea ice boundary dataset for the Community Atmosphere Model. *J. Climate*, **21**, 5145–5153, https://doi.org/10.1175/2008JCLI2292.1.

IPCC, 2023: The Earth's energy budget, climate feedbacks and climate sensitivity. *Climate Change 2021: The Physical Science Basis*, V. Masson-Delmotte et al., Eds., Cambridge University Press, 923–1054, https://doi.org/10.1017/9781009157896.009.

Khairoutdinov, M., and Y. Kogan, 2000: A new cloud physics parameterization in a large-eddy simulation model of marine stratocumulus. *Mon. Wea. Rev.*, **128**, 229–243, https://doi.org/10.1175/1520-0493(2000)128<0229:ANCPPI>2.0.CO;2.

Klein, S. A., A. Hall, J. R. Norris, and R. Pincus, 2017: Low-cloud feedbacks from cloud-controlling factors: A review. *Surv. Geophys.*, **38**, 1307–1329, https://doi.org/10.1007/s10712-017-9433-3.

Larson, V. E., and J.-C. Golaz, 2005: Using probability density functions to derive consistent closure relationships among higher-order moments. *Mon. Wea. Rev.*, **133**, 1023–1042, https://doi.org/10.1175/MWR2902.1.

Liu, X., P.-L. Ma, H. Wang, S. Tilmes, B. Singh, R. C. Easter, S. J. Ghan, and P. J. Rasch, 2016: Description and evaluation of a new four-mode version of the Modal Aerosol Module (MAM4) within version 5.3 of the Community Atmosphere Model. *Geosci. Model Dev.*, **9**, 505–522, https://doi.org/10.5194/gmd-9-505-2016.

Loeb, N. G., and Coauthors, 2018: Clouds and the Earth's Radiant Energy System (CERES) Energy Balanced And Filled (EBAF) top-of-atmosphere (TOA) edition-4.0 data product. *J. Climate*, **31**, 895–918, https://doi.org/10.1175/JCLI-D-17-0208.1.

Ma, P.-L., and Coauthors, 2022: Better calibration of cloud parameterizations and subgrid effects increases the fidelity of the E3SM Atmosphere Model version 1. *Geosci. Model Dev.*, **15**, 2881–2916, https://doi.org/10.5194/gmd-15-2881-2022.

McCoy, D. T., and Coauthors, 2022: Extratropical shortwave cloud feedbacks in the context of the global circulation and hydrological cycle. *Geophys. Res. Lett.*, **49**, e2021GL097154, https://doi.org/10.1029/2021GL097154.

——, M. E. Frazer, J. Mülmenstädt, I. Tan, C. R. Terai, and M. D. Zelinka, 2023: Extratropical cloud feedbacks. *Clouds and their Climatic Impacts: Radiation, Circulation, and Precipitation*, *Geophys. Monogr.*, Vol. **281**, Amer. Geophys. Union, 133–157, https://doi.org/10.1002/9781119700357.ch6.

McKim, B., S. Bony, and J.-L. Dufresne, 2024: Weak anvil cloud area feedback suggested by physical and observational constraints. *Nat. Geosci.*, **17**, 392–397, https://doi.org/10.1038/s41561-024-01414-4.

Medeiros, B., J. Shaw, J. E. Kay, and I. Davis, 2023: Assessing clouds using satellite observations through three generations of global atmosphere models. *Earth Space Sci.*, **10**, e2023EA002918, https://doi.org/10.1029/2023EA002918.

Meraner, K., T. Mauritsen, and A. Voigt, 2013: Robust increase in equilibrium climate sensitivity under global warming. *Geophys. Res. Lett.*, **40**, 5944–5948, https://doi.org/10.1002/2013GL058118.

Mitchell, J. F. B., C. A. Senior, and W. J. Ingram, 1989: CO_2 and climate: A missing feedback? *Nature*, **341**, 132–134, https://doi.org/10.1038/341132a0.

Mülmenstädt, J., and Coauthors, 2021: An underestimated negative cloud feedback from cloud lifetime changes. *Nat. Climate Change*, **11**, 508–513, https://doi.org/10.1038/s41558-021-01038-1.

Myers, T. A., and J. R. Norris, 2013: Observational evidence that enhanced subsidence reduces subtropical marine boundary layer cloudiness. *J. Climate*, **26**, 7507–7524, https://doi.org/10.1175/JCLI-D-12-00736.1.

Qu, X., A. Hall, S. A. Klein, and P. M. Caldwell, 2015a: The strength of the tropical inversion and its response to climate change in 18 CMIP5 models. *Climate Dyn.*, **45**, 375–396, https://doi.org/10.1007/s00382-014-2441-9.

——, ——, ——, and A. M. DeAngelis, 2015b: Positive tropical marine low-cloud cover feedback inferred from cloud-controlling factors. *Geophys. Res. Lett.*, **42**, 7767–7775, https://doi.org/10.1002/2015GL065627.

Richter, I., and S.-P. Xie, 2008: Muted precipitation increase in global warming simulations: A surface evaporation perspective. *J. Geophys. Res.*, **113**, D24118, https://doi.org/10.1029/2008JD010561.

Rieck, M., L. Nuijens, and B. Stevens, 2012: Marine boundary layer cloud feedbacks in a constant relative humidity atmosphere. *J. Atmos. Sci.*, **69**, 2538–2550, https://doi.org/10.1175/JAS-D-11-0203.1.

Rossow, W. B., K. R. Knapp, and A. H. Young, 2022: International satellite cloud climatology project: Extending the record. *J. Climate*, **35**, 141–158, https://doi.org/10.1175/JCLI-D-21-0157.1.

Schneider, T., P. A. O'Gorman, and X. J. Levine, 2010: Water vapor and the dynamics of climate changes. *Rev. Geophys.*, **48**, RG3001, https://doi.org/10.1029/2009RG000302.

——, C. M. Kaul, and K. G. Pressel, 2019: Possible climate transitions from breakup of stratocumulus decks under greenhouse warming. *Nat. Geosci.*, **12**, 163–167, https://doi.org/10.1038/s41561-019-0310-1.

Scott, R. C., T. A. Myers, J. R. Norris, M. D. Zelinka, S. A. Klein, M. Sun, and D. R. Doelling, 2020: Observed sensitivity of low-cloud radiative effects to meteorological perturbations over the global oceans. *J. Climate*, **33**, 7717–7734, https://doi.org/10.1175/JCLI-D-19-1028.1.

Shaw, J., Z. McGraw, O. Bruno, T. Storelvmo, and S. Hofer, 2022: Using satellite observations to evaluate model representation of Arctic mixed-phase clouds. *Geophys. Res. Lett.*, **49**, e2021GL096191, https://doi.org/10.1029/2021GL096191.

Sherwood, S. C., and Coauthors, 2020: An assessment of Earth's climate sensitivity using multiple lines of evidence. *Rev. Geophys.*, **58**, e2019RG000678, https://doi.org/10.1029/2019RG000678.

Soden, B. J., I. M. Held, R. Colman, K. M. Shell, J. T. Kiehl, and C. A. Shields, 2008: Quantifying climate feedbacks using radiative kernels. *J. Climate*, **21**, 3504–3520, https://doi.org/10.1175/2007JCLI2110.1.

Sokol, A. B., C. J. Wall, and D. L. Hartmann, 2024: Greater climate sensitivity implied by anvil cloud thinning. *Nat. Geosci.*, **17**, 398–403, https://doi.org/10.1038/s41561-024-01420-6.

Stephens, G. L, 1978: Radiation profiles in extended water clouds. II: Parameterization schemes. *J. Atmos. Sci.*, **35**, 2123–2132, https://doi.org/10.1175/1520-0469(1978)035<2123:RPIEWC>2.0.CO;2.

Tan, I., T. Storelvmo, and M. D. Zelinka, 2016: Observational constraints on mixed-phase clouds imply higher climate sensitivity. *Science*, **352**, 224–227, https://doi.org/10.1126/science.aad5300.

Taylor, K. E., M. Crucifix, P. Braconnot, C. D. Hewitt, C. Doutriaux, A. J. Broccoli, J. F. B. Mitchell, and M. J. Webb, 2007: Estimating shortwave radiative forcing and response in climate models. *J. Climate*, **20**, 2530–2543, https://doi.org/10.1175/JCLI4143.1.

Tierney, J. E., and Coauthors, 2020: Past climates inform our future. *Science*, **370**, eaay3701, https://doi.org/10.1126/science.aay3701.

Vecchi, G. A., and B. J. Soden, 2007: Global warming and the weakening of the tropical circulation. *J. Climate*, **20**, 4316–4340, https://doi.org/10.1175/JCLI4258.1.

Vial, J., J.-L. Dufresne, and S. Bony, 2013: On the interpretation of inter-model spread in CMIP5 climate sensitivity estimates. *Climate Dyn.*, **41**, 3339–3362, https://doi.org/10.1007/s00382-013-1725-9.

Wang, Y., X. Liu, C. Hoose, and B. Wang, 2014: Different contact angle distributions for heterogeneous ice nucleation in the Community Atmospheric Model version 5. *Atmos. Chem. Phys.*, **14**, 10 411–10 430, https://doi.org/10.5194/acp-14-10411-2014.

Webb, M. J., A. P. Lock, and F. H. Lambert, 2018: Interactions between hydrological sensitivity, radiative cooling, stability, and low-level cloud amount feedback. *J. Climate*, **31**, 1833–1850, https://doi.org/10.1175/JCLI-D-16-0895.1.

——, ——, and T. Ogura, 2024: What are the main causes of positive subtropical low cloud feedbacks in climate models? *J. Adv. Model. Earth Syst.*, **16**, e2023MS003716, https://doi.org/10.1029/2023MS003716.

Wood, R., and C. S. Bretherton, 2006: On the relationship between stratiform low cloud cover and lower-tropospheric stability. *J. Climate*, **19**, 6425–6432, https://doi.org/10.1175/JCLI3988.1.

Zelinka, M. D., D. A. Randall, M. J. Webb, and S. A. Klein, 2017: Clearing clouds of uncertainty. *Nat. Climate Change*, **7**, 674–678, https://doi.org/10.1038/nclimate3402.

——, T. A. Myers, D. T. McCoy, S. Po-Chedley, P. M. Caldwell, P. Ceppi, S. A. Klein, and K. E. Taylor, 2020: Causes of higher climate sensitivity in CMIP6 models. *Geophys. Res. Lett.*, **47**, e2019GL085782, https://doi.org/10.1029/2019GL085782.

——, S. A. Klein, Y. Qin, and T. A. Myers, 2022: Evaluating climate models' cloud feedbacks against expert judgment. *J. Geophys. Res. Atmos.*, **127**, e2021JD035198, https://doi.org/10.1029/2021JD035198.

Zhang, G. J., and N. A. McFarlane, 1995: Sensitivity of climate simulations to the parameterization of cumulus convection in the Canadian climate centre general circulation model. *Atmos.–Ocean*, **33**, 407–446, https://doi.org/10.1080/07055900.1995.9649539.

Zhao, X., and Coauthors, 2023: Important ice processes are missed by the Community Earth System Model in Southern Ocean mixed-phase clouds: Bridging SOCRATES observations to model developments. *J. Geophys. Res. Atmos.*, **128**, e2022JD037513, https://doi.org/10.1029/2022JD037513.

Zhou, C., M. D. Zelinka, and S. A. Klein, 2016: Impact of decadal cloud variations on the Earth's energy budget. *Nat. Geosci.*, **9**, 871–874, https://doi.org/10.1038/ngeo2828.

Zhu, J., and C. J. Poulsen, 2020: On the increase of climate sensitivity and cloud feedback with warming in the Community Atmosphere Models. *Geophys. Res. Lett.*, **47**, e2020GL089143, https://doi.org/10.1029/2020GL089143.

——, and ——, 2021: Last Glacial Maximum (LGM) climate forcing and ocean dynamical feedback and their implications for estimating climate sensitivity. *Climate Past*, **17**, 253–267, https://doi.org/10.5194/cp-17-253-2021.

——, ——, and J. E. Tierney, 2019: Simulation of Eocene extreme warmth and high climate sensitivity through cloud feedbacks. *Sci. Adv.*, **5**, eaax1874, https://doi.org/10.1126/sciadv.aax1874.

——, ——, and B. L. Otto-Bliesner, 2020: High climate sensitivity in CMIP6 model not supported by paleoclimate. *Nat. Climate Change*, **10**, 378–379, https://doi.org/10.1038/s41558-020-0764-6.

——, B. L. Otto-Bliesner, E. C. Brady, C. J. Poulsen, J. E. Tierney, M. Lofverstrom, and P. DiNezio, 2021: Assessment of equilibrium climate sensitivity of the Community Earth System Model version 2 through simulation of the last glacial maximum. *Geophys. Res. Lett.*, **48**, e2020GL091220, https://doi.org/10.1029/2020GL091220.

——, and Coauthors, 2022: LGM paleoclimate constraints inform cloud parameterizations and equilibrium climate sensitivity in CESM2. *J. Adv. Model. Earth Syst.*, **14**, e2021MS002776, https://doi.org/10.1029/2021MS002776.

——, C. J. Poulsen, and B. L. Otto-Bliesner, 2024: Modeling past hothouse climates as a means for assessing Earth system models and improving the understanding of warm climates. *Annu. Rev. Earth Planet. Sci.*, **52**, 351–378, https://doi.org/10.1146/annurev-earth-032320-100333.